Review

Review of Preparation and Performance of Micro-Arc Oxidation Coatings on Various Metal Substrates

Ningning Li , Huiyi Wang , Qiuzhen Liu , Zhenjie Hao , Da Xu , Xi Chen , Datian Cui , Lei Xu * , Yaya Feng *

Posted Date: 16 September 2025

doi: 10.20944/preprints202509.1363.v1

Keywords: micro-arc oxidation; wear resistance; bonding strength; long-term stability

 doi:10.20944/preprints202509.1363.v1

Review

Review of Preparation and Performance of Micro-Arc Oxidation Coatings on Various Metal Substrates

Ningning Li [1,2], Huiyi Wang [1], Qiuzhen Liu [3], Zhenjie Hao [1], Da Xu [1], Xi Chen [1], Datian Cui [1], Lei Xu [1,*] and Yaya Feng [4,*]

[1] School of Materials Science and Engineering, North China University of Water Resources and Electric Power, Zhengzhou 450045, China

[2] Luoyang Aijia Mold Manufacturing Co., Ltd, Luoyang, 471000, China

[3] Zhengzhou Jintai Can Manufacturing Co., Ltd, Zheng zhou, 450007, China

[4] National Key Laboratory of Aerospace Chemical Power, Inner Mongolia Research Institute of Synthetic Chemical Industry, Hohhot, 010010, China

* Correspondence: xulei2022@ncwu.edu.cn (L.X.); fengyaya0127@163.com (Y.F.)

Abstract

Micro-arc oxidation (MAO) technology demonstrates remarkable advantages in fabricating ceramic coatings on lightweight alloys. For aluminum alloys, MAO rapidly forms dense, pore-free ceramic layers within minutes, significantly enhancing corrosion and wear resistance at low processing costs. In magnesium alloys, optimized electrolyte compositions and process parameters enable composite coatings with combined high hardness and self-lubrication properties, while post-treatments like laser melting or corrosion inhibitors extend salt spray corrosion resistance. Titanium alloys benefit from MAO coatings with exceptional interfacial bonding strength and mechanical performance, making them ideal for biomedical implants and aerospace components. Notably, dense ceramic oxide films grown in-situ via MAO on high-entropy alloys (HEAs) triple surface hardness and enhance wear/corrosion resistance. However, MAO applications on steel require pre-treatments like aluminizing, thermal spraying, or ion plating. Current challenges include coating uniformity control, efficiency for complex geometries, and long-term stability. Future research focuses on multifunctional coatings (self-healing, antibacterial) and eco-friendly electrolyte systems to expand engineering applications.

Keywords: micro-arc oxidation; wear resistance; bonding strength; long-term stability

1. Introduction

Micro-arc oxidation (MAO), also known as Plasma Electrolytic Oxidation (PEO), is an electrochemical surface modification technique that generates in situ ceramic coatings on metal substrates through high voltage induced micro-discharges [1]. During MAO, localized plasma discharges at the metal-electrolyte interface facilitate the oxidation of metal ions, forming dense oxide or composite ceramic layers. This process is characterized by its simplicity, environmental friendliness, and strong coating-substrate adhesion. Currently, MAO has achieved industrial scale applications in lightweight alloys (e.g., aluminum, magnesium, and titanium alloys) for corrosion protection and functionalization [2–4]. The schematic diagram of the micro arc oxidation device and process flow is shown in Figure 1.

However, challenges such as coating uniformity, processing efficiency for complex geometries, and long-term stability under harsh environments remain unresolved. Recent research has expanded to high-entropy alloys (HEAs) [5], driven by demands for advanced multifunctional coatings in aerospace, biomedical, and energy sectors.

 doi:10.20944/preprints202509.1363.v1

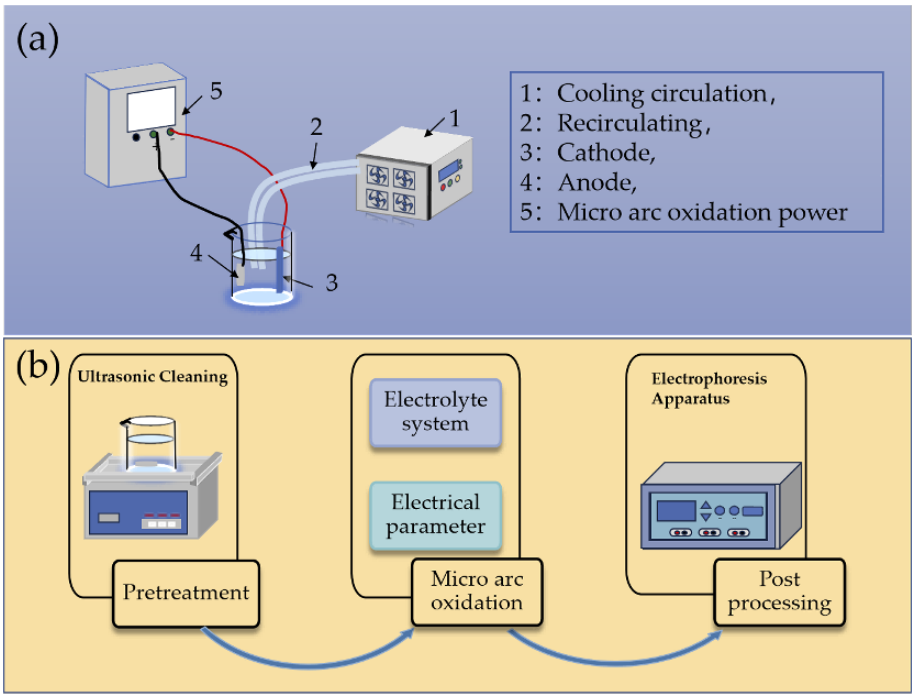

Figure 1. Schematic diagram of micro arc oxidation device (a) and process flow (b).

Aluminum alloys benefit from MAO through rapid formation (within minutes) of dense, pore free Al_2O_3-based ceramic layers (10–100 μm thickness) with hardness values of HV 1000–1500. The polished α-Al_2O_3 dominant coating demonstrated a wear rate of 3.00–5.00×10^{-6} mm^3/N·m under 2 MPa contact pressure, achieved an antiwear life of 2500 m (1.25 m/s, 300 N) with a friction coefficient >0.45 in Timken testing [6]. Composite coatings on AZ91D magnesium alloy, fabricated through MAO followed by low-pressure multi-immersion sealing, demonstrated significantly enhanced corrosion resistance compared to standalone MAO films. This barrier mechanism stems from the sealing agent's obstruction of transport pathways within the MAO structure [7]. Sun et al. [8] studied varying anodic (j_a) and cathodic (j_c) current densities MAO coating characteristics on Ti–6Al–4V alloy. Higher j_a accelerated anodic voltage rise, increased coating thickness, and coarsened surface morphology, while elevated j_c reduced growth rates and enhanced structural uniformity. Elemental distribution shifts across the coatings, driven by Ti dissolution and electromigration of charged species like $Al(OH)_4^-$, were linked to j_a/j_c variations, as confirmed by XRD, EDS, and cross-sectional analyses. These findings highlight the critical role of current density balance in tailoring MAO coating properties.

The multi-principal element nature of HEAs necessitates tailored electrolyte design for MAO. For example, this study developed a MAO process for AlCoCrFeNi high-entropy alloys with low valve metal content, optimizing sintering temperatures to achieve high performance HEAs-MAO coatings. The coatings, primarily composed of Al_2O_3 with trace Co, Fe, and Ni oxides (notably Co_3O_4, causing surface blue spots), were characterized via SEM, XRD, and EDS. The HEA7-M sample exhibited a thicker coating, reduced friction coefficient, enhanced hardness, and superior wear/corrosion resistance compared to uncoated HEA7, validated by tribological and electrochemical tests [9].

Direct MAO on steel is hindered by its high conductivity and low oxidation potential. Effective pre-treatments include: (1) Aluminizing, a composite coating composed of intermetallic compounds, Al–Si alloys, and an oxide ceramic layer was prepared on TA2 substrate by hot-dipping Al–Si alloy and MAO [10]; (2) Thermal spraying, for example, a double-layer coating technique, which consisted of a thermal sprayed titanium (Ti) layer and a MAO film on AISI 1020 steel [11]; (3) Laser cladding, the composite coating exhibited superior interfacial adhesion to the substrate and demonstrated enhanced mechanical performance characteristics [12]. These hybrid approaches expand MAO's

 doi:10.20944/preprints202509.1363.v1

applicability to steel components like cutting tools and bearings, bridging the gap between lightweight and high-strength materials.

Based on the information retrieved with the keywords "Micro-arc oxidation" in the Web of Science database, as shown in Figure 2, more than 3195 relevant articles on the topic of MAO have been published in the past 22 years, and the citation frequency of relevant additive manufacturing literature is increasing year by year, accumulated to nearly 90000 times. In this review, comprehensively analyzes MAO advancements across aluminum, magnesium, titanium, and high-entropy alloys, as well as steel. It elucidates coating formation mechanisms, performance optimization strategies, and engineering limitations, with emphasis on electrolyte design, process parameter control, and hybrid modification techniques. By synthesizing recent innovations, this work aims to provide theoretical foundations for developing multifunctional MAO coatings (e.g., self healing, antibacterial) and eco-friendly processes, ultimately accelerating their adoption in aerospace, biomedical devices, and energy infrastructure. The findings are expected to guide future research toward addressing scalability and durability challenges in industrial applications.

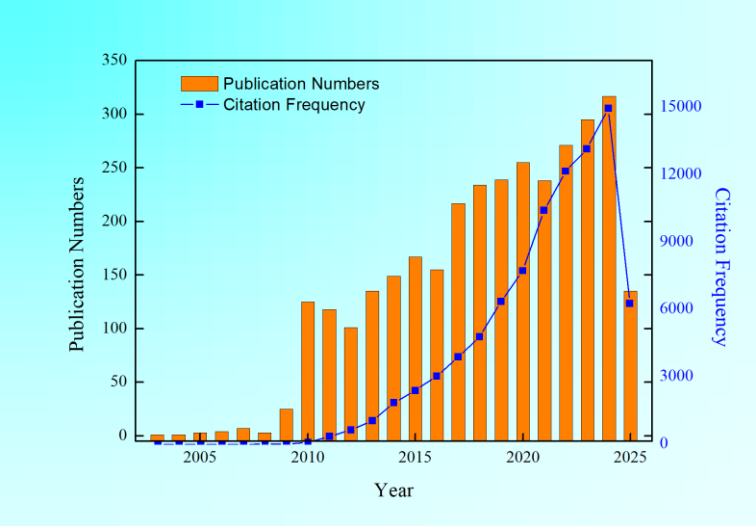

Figure 2. The histogram of publication numbers and citation frequency with the keywords "Micro-arc oxidation" retrieved from Web of Science database.

2. MAO Treatment Technology for Various Metallic Materials

The MAO processing techniques diverge considerably across different metallic materials, with material specific optimization protocols and prioritized performance metrics. The following sections will provide detailed elucidations on these aspects.

2.1. MAO Treatment Technology for Al-Based Alloys

MAO of Al-based alloys is an advanced surface treatment technology that in-situ grows a ceramic oxide film on the aluminum alloy surface [13–15]. Its principle involves applying high voltage and high current to break through the Faraday region of conventional anodization, generating micro-arc plasma discharge on the metal surface [16–18]. This causes complex reactions, including melting, sintering, and phase transformation of the aluminum substrate, ultimately forming a ceramic layer. This layer is primarily composed of α-Al_2O_3 (corundum phase), characterized by a dense structure, high hardness, and strong adhesion strength [19–21].

Current density is a critical factor influencing the micro-arc oxidation treatment of aluminum alloys [22–24]. Yang et al. [25] conducted experiments on aluminum-based alloys using a Na_2SiO_3 electrolyte under current densities ranging from 3 to 25 A/dm². Their findings revealed: High current density (>10 A/dm²): The coating predominantly consists of α-Al_2O_3 (high hardness), driven by the

 doi:10.20944/preprints202509.1363.v1

elevated temperature (~10,000 K) in discharge channels. Low current density (<10 A/dm²): The coating primarily forms γ-Al_2O_3. Coating thickness increases with current density, but higher current density leads to non-uniform pore distribution, causing uneven hardness (up to 2500 HV). Wang et al. [26] investigated MAO treatment on 7E04 aluminum drillpipe material in an electrolyte containing SiC particles under current densities of 1–20 A/dm², the specific electrolyte composition is detailed in Table 1. Key results include: Increased current density raises oxidation voltage and coating thickness (2.66 μm at 1 A/dm² *vs*. 14.81 μm at 20 A/dm²). High current density induces rougher surfaces and larger pore sizes (1–10 μm), reducing micro-hardness (peak hardness at 1 A/dm² decreases at 20 A/dm²). SiC oxidation generates SiO_2, enhancing corrosion resistance, but increased porosity partially counteracts this benefit.

Table 1. The specific electrolyte composition of MAO treatment on 7E04 aluminum drillpipe material [26].

Component	Concentration/Dosage	Remarks
Sodium Silicate (Na_2SiO_3)	15 g/L	Acts as a silicon source, participates in alumina coating formation.
Sodium Hydroxide (NaOH)	1 g/L	Adjusts electrolyte pH and enhances conductivity.
Glycerol ($C_3H_8O_3$)	2 mL/L	Serves as a dispersant and stabilizer, ensuring uniform mixing.
Silicon Carbide (SiC) Particles	3 g/L	Particle size ~50 μm; continuous stirring required to maintain suspension.

Scholars have systematically investigated the effects of cathodic-to-anodic current ratio [27], hybrid voltage (DC+AC) [28], and electrolyte composition on coating properties [26]. The findings reveal that elevated cathodic current density promotes densification layer thickening and porosity reduction [27]. Hybrid voltage coatings exhibit superior corrosion resistance compared to pure DC counterparts, with more uniform pore distribution (<1 μm) [28]. When implementing MAO in Na_2SiO_3-NaOH electrolyte containing 3 g/L SiC particles, SiC oxidation to SiO_2 was observed to enhance corrosion resistance, though excessive current density induced porosity increment compromised performance. Incorporation of Na_2WO_4 in the electrolyte effectively reduces breakdown voltage and improves coating densification.

In their mechanistic investigation of micro-arc oxidation (MAO) on 6061 aluminum alloy utilizing a Na_2SiO_3-CH_3COONa-$Na_5P_3O_{10}$ electrolyte system, Li et al. [29] demonstrated that micro-arc discharges are sequentially initiated at the coating-substrate interface, thereby forming spark clusters. The ejection of molten metal results in the generation of characteristic molten pools, whose diameters exhibit a linear correlation with coating thickness. Structural analyses revealed the following findings: (1) The coating is composed of α-Al_2O_3 and γ-Al_2O_3 phases, with the α-phase content progressively increasing from the surface toward the substrate interface; (2) Trumpet shaped molten pools interconnect to form three-dimensional pore networks; (3) Discharge induced micro-pores located at the coating base have a diameter range of 150-200 nm.

Researchers have explored the incorporation of various additives into electrolytes to enhance MAO coating performance. For instance, Jin et al [30] introduced Fe micrograins (several μm in diameter) into a Na_2SiO_3-NaOH electrolyte to fabricate Fe-Al_2O_3 composite coatings on LY2 aluminum alloy. Results demonstrated that Fe micrograins optimized discharge channel reactions (e.g., diffusion and electrophoresis), reducing porosity and improving mechanical properties. Figure 3a displays the surface morphology of the MAO Al_2O_3 coatings with and without Fe micrograins obtained by SEM, the XRD spectra obtained from MAO coatings with and without Fe micrograins are presented in Figure 3b. the surface roughness of the samples was further characterized using a surface texture tester, with the results presented in Figure 3c. Based on the changes in morphology, composition, and roughness, it can be observed that a large number of Fe micrograins are embedded

 doi:10.20944/preprints202509.1363.v1

into the Al_2O_3 coatings through diffusion and electrophoresis, and the density of these coatings is significantly higher compared to those without Fe micrograins.

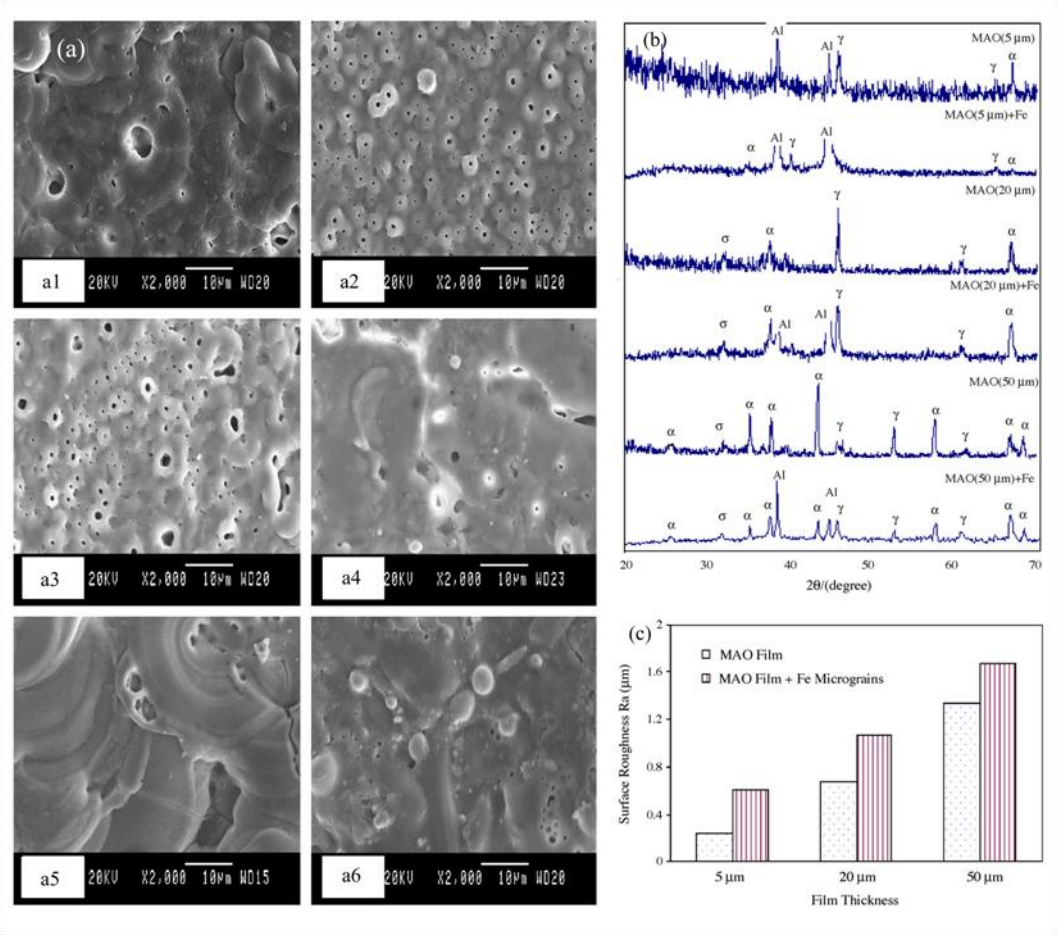

Figure 3. Improvement of surface porosity and properties of alumina films by incorporation of Fe micrograins in micro-arc oxidation. (a) Surface morphology of the MAO Al_2O_3 coating of different thicknesses with and without Fe micrograins: (a1) 5 mm coating without Fe; (a2) 5 mm coating with Fe; (a3) 20 mm coating without Fe; (a4) 20 mm coating with Fe; (a5) 50 mm coating without Fe; (a6) 50 mm coating with Fe. (b) XRD spectra acquired from the MAO Al_2O_3 coatings of different thicknesses with and without Fe micrograins. (c) Relationship between the average surface roughness (R_a) and MAO Al_2O_3 coating thickness with and without Fe micrograins [30].

Li et al. [31] investigated the growth mechanisms of MAO coatings on 2A70 aluminum alloy using a two-step oxidation method (silicate → phosphate or phosphate → silicate). In silicate electrolytes, "dumbbell-shaped" discharge channels restricted reactive zones but introduced more electrolyte, leading to island-like growth. Conversely, in phosphate electrolytes, "trumpet-shaped" discharge channels facilitated heat accumulation and inward reaction propagation, resulting in layered growth. Post-oxidation, localized Si-rich regions formed in silicate electrolytes, while continuous P-Al_2O_3 layers emerged in phosphate electrolytes, highlighting the critical role of electrolyte composition in regulating discharge dynamics and coating morphology.

Chen et al. [32] incorporated graphene particles (0–0.2 g/L) into a Na_2SiO_3-based electrolyte to prepare graphene-Al_2O_3 composite coatings, the XRD phase results are shown in Figure 4a. Optimal performance was achieved at 0.15 g/L graphene: coating thickness reached 11.7 μm, microhardness increased to 226.84 HV, as shown in Figure 4b, and porosity dropped to 12.4% (See Figure 4c.) due to graphene embedding and pore sealing. After 530 hours of salt spray testing, mass loss was only 1.5 mg/cm², significantly outperforming the unmodified coating (3.1 mg/cm²), see Figure 4d for details. Moderate graphene addition enhanced conductivity and accelerated molten ejecta solidification,

 doi:10.20944/preprints202509.1363.v1

improving densification and corrosion resistance, while excessive graphene induced cracks, compromising performance [32].

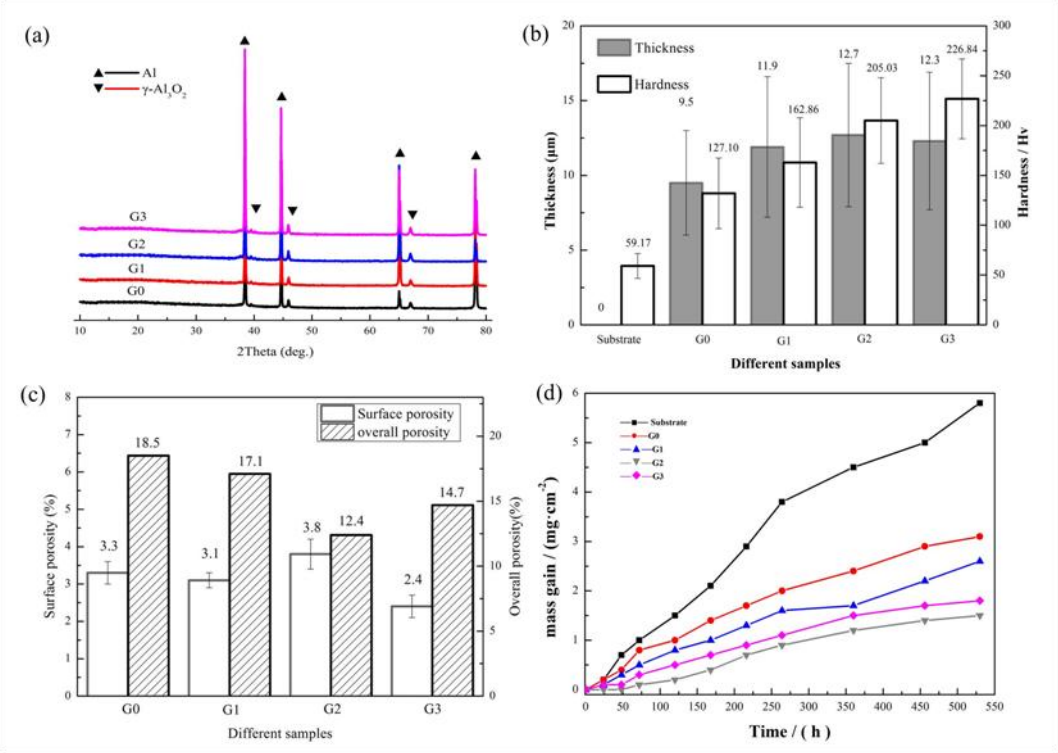

Figure 4. Influence of graphene particles on the micro-arc oxidation behaviors of 6063 aluminum alloy and the coating properties. (a) XRD patterns of different samples, (b) Porosity of different samples, (c) Thickness and hardness of different samples, (d) Mass gain of the coating samples during salt spray test [32].

The phase composition of the MAO coating consists of a dense, high-hardness inner α-Al_2O_3 layer and a porous, low-density outer γ-Al_2O_3 layer [6]. Performance investigations encompass friction wear [33], impact wear [34], corrosion (including stress corrosion) [35], fatigue [2], and high-temperature behavior [36]. Arslan et al. [33] demonstrated that polished MAO coatings exhibit low wear rates ($3.00–5.00 \times 10^{-6}$ $mm^3/N·m$) and stable friction coefficients (0.45–0.6) under ceramic-on-abrasion conditions, with further friction reduction observed at 200°C. The MAO coating significantly reduces wear volume by absorbing impact energy (with energy absorption ratios exceeding those of the substrate) [34]. While increased coating thickness enhances wear resistance, excessive thickness may induce fatigue cracks due to residual stresses. MAO coatings improve impedance values by 1-2 orders of magnitude in 3.5% NaCl solution, effectively suppressing localized corrosion (Venugopal et al.) [35]. Pre-treatments like thermal oxidation further enhance corrosion resistance through structural optimization. The coating notably delays stress corrosion failure in aluminum alloys: uncoated specimens failed within 30 days under 80% yield strength, while coated specimens maintained high elongation (10.5%) [35]. Micro-defects (pores, cracks) and residual stresses constitute primary fatigue failure mechanisms. Process optimizations such as gradient current and post-treatment polishing can extend fatigue life [2]. MAO coatings maintain integrity under 873 K thermal shock, though thermal expansion coefficient mismatch (7.38×10^{-6} K^{-1}) induces thermal stress without observable cracking [36].

The performance of micro-arc oxidation is synergistically influenced by multiple parameters (current mode, ultrasonic power, electrolyte flow rate), with optimized parameter combinations being crucial for enhancing coating properties. Recent studies include the work by Ma et al. [37] on 17% SiC particle-reinforced aluminum matrix composites (17% SiCp/2009 AMC), which combined experimental analysis with density functional theory (DFT) simulations to elucidate the growth mechanisms and product formation processes of micro-arc oxidation coatings. Scholars have

 doi:10.20944/preprints202509.1363.v1

summarized the MAO oxidized ceramic film's growth mechanism diagram, specifically, as shown in Figure 5, mainly includes the schematic diagram of reaction mechanism for SiC oxidation, and the changes after adding $Ce(NO_3)_3 \cdot 6H_2O$ [37].

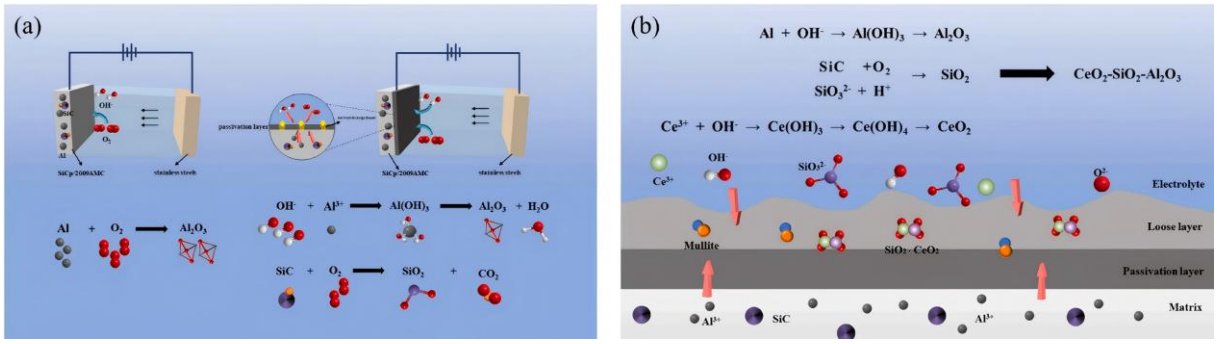

Figure 5. Growth mechanism diagram of the MAO oxidized ceramic film. (a) Schematic diagram of reaction mechanism. (b) Schematic diagram of the film-forming mechanism of $Ce(NO_3)_3 \cdot 6H_2O$ addition [37].

Liu et al. [38] investigated the effects of ultrasonic power (0-90 W) assisted micro-arc oxidation on the microstructure and properties of 6061 aluminum alloy coatings, revealing that at 50 W ultrasonic power (abbreviated as U-50), the cross-sectional micromorphology and EDS spectra are shown in Figure 6a, the coating achieved maximum hardness (approximately 240 HV), minimum porosity (1.88%), and optimal wear resistance and corrosion resistance. Figure 6b shows the equivalent circuit diagram, and the sample U-50 has the best fitting degree. Figure 6c illustrates the growth mechanism of the MAO coating under ultrasonic assistance. In the pre-growth phase of the coating, microflow and emission waves generated by ultrasound increase the number of charged particles in the solution and accelerate their migration, thereby enhancing the coating's growth rate. Scanning micro-arc oxidation (SMAO) technology overcomes traditional size limitations through dynamic parameter control (e.g., robotic arm manipulation), enabling efficient processing of complex-shaped components [39,40].

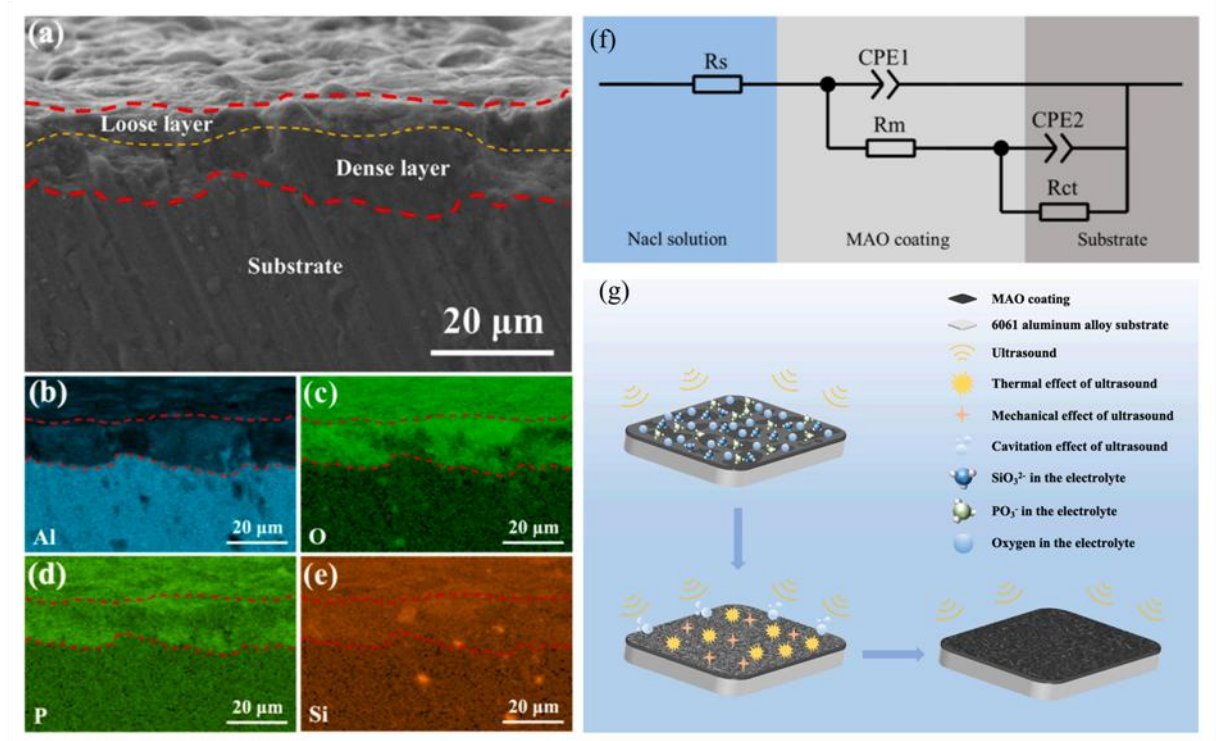

Figure 6. Influence of ultrasonic power modulation on the optimisation of aluminium alloy micro-arc oxidation coating properties. (a) cross-sectional morphology of sample U-50; EDS spectra of sample U-50: (b) elemental Al,

 doi:10.20944/preprints202509.1363.v1

(c) elemental O, (d) elemental P and (e) elemental Si; (f) Equivalent circuit diagram of coated specimen: R_s represents the solution resistance, R_m stands for the coating resistance, R_{ct} refers to the charge transfer resistance, and the two CPEs are the capacitive elements between different interfaces; (g) Growth mechanism of MAO coating under ultrasound assistance [38].

2.2. MAO Treatment Technology for Mg-Based Alloys

Similarly, MAO of Mg-based alloys, based on the principle of plasma electrolytic oxidation, is an advanced technology for directly synthesizing ceramic coatings on the surface of magnesium alloys [41–43]. This process occurs under high voltage and strong current conditions, surpassing the limitations of conventional anodization and inducing intense micro-discharge phenomena on the magnesium alloy substrate [44–46]. During this process, intense plasma chemical reactions occur, causing the magnesium substrate to undergo melting, oxidation, and sintering, ultimately resulting in the in-situ formation of a ceramic layer. This layer is primarily composed of MgO (periclase) and complex spinel-type composite oxides [47–49]. The resulting dense ceramic structure significantly enhances the key properties of magnesium alloys, particularly highlighting its unique advantage in the biomedical field—biocompatibility [50–52].

The performance of MAO coatings on Mg alloys is synergistically regulated by electrolyte composition (e.g., silicates, Hydroxyapatite (HA) precursors), current mode (bipolar pulses), and voltage. Parameter optimization is critical for enhancing coating densification and functionality [53–56], and the MAO electrolyte compositions are listed in Table 2 [53–55]. Zhang et al. [55] studied the dynamic coating formation on dual-phase AZ91HP Mg alloy (α-Mg + β-$Mg_{17}Al_{12}$) in a neutral electrolyte. The coatings preferentially nucleated at α-phase edges before expanding to β-phase, eventually covering the entire surface. This work elucidated the heterogeneous distribution of microarc discharges in dual-phase alloys, providing theoretical insights for surface treatment of multiphase materials.

Table 2. The MAO electrolyte compositions for Mg-based alloys of Refs [53–55].

	Ingredients	Concentration		Ingredients	Concentration
Ref 53	$NaAlO_2$	9 g/L	Ref 55	$C_6H_{18}O_{24}P_6$	5 g/L
	KF	6 g/L		HF(40%)	20 g/L
Ref 54	Na_2SiO_3	6 g/L		H_3PO_4(98%)	58 g/L
	KF	2 g/L		H_3BO_3	35 g/L
	KOH	2 g/L		Hexamethylenetetramine	360 g/L
	$C_3H_8O_3$	10 mL/L		PH regulator	pH=7.0

Tang et al. [56] synthesized HA-containing MAO coatings in a calcium glycerophosphate-based electrolyte by adjusting voltages (250–500 V). Figure 7a shows that MAO coating thickness and surface roughness increase with applied voltage. Below 400V, thickness grows slowly and linearly; above 400V, it rises sharply. Roughness exhibits a similar voltage dependent trend. Higher instantaneous energy accelerates MAO coating growth, consistent with previous studies. At 400 V, the coatings achieved superior hydrophobicity (contact angle 128 °), as shown in Figure 7b. As shown in Figure 7c, the corrosion current of the maintained oxide film layer prepared under 400V is presented, with the corrosion current density of 1.06×10^{-7} A/cm² in SBF solution. As illustrated in Figure 7d, this kinetic difference leads to the sequential adsorption of ions on the Mg anode surface: OH^- first encapsulates the anode, followed by PO_4^{3-} and calcium ions. The preferential participation of OH^- in micro-discharge reactions, succeeded by PO_4^{3-} and calcium ions, aligns with the elemental distribution observed in the MAO coatings.

 doi:10.20944/preprints202509.1363.v1

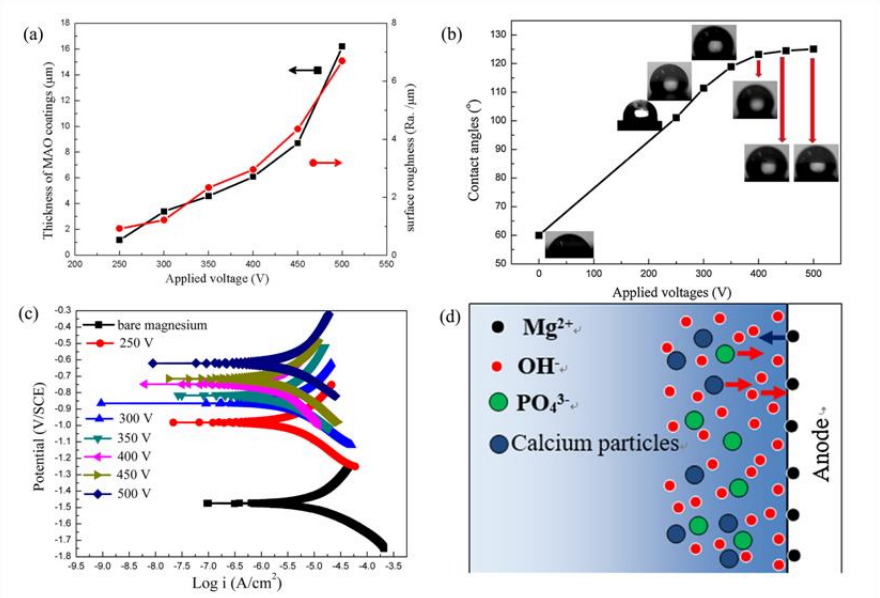

Figure 7. Synthesis and properties of hydroxyapatite-containing coating on AZ31 magnesium alloy by micro-arc oxidation. (a) Variation of thickness and roughness of MAO coatings formed with different applied voltages, (b) Contact angles on the surface of bare AZ31 Mg alloy and MAO coatings, (c) Polarization curves of bare magnesium and the MAO coatings, (d)Schematic illustration of the ion distribution on the surface of the Mg anode during MAO process [56].

The performance of MAO technology in surface treatment of magnesium alloys includes corrosion resistance [57–60], mechanical properties [61–63], biocompatibility and degradation behavior [64,65], and high-temperature oxidation resistance [66]. The solution systems used for its corrosion resistance include aluminate fluoride system [57], silicate system [58,59], and phosphate system [60]. In the aluminate fluoride system, an $MgAl_2O_4$ spinel phase coating formed on AZ91D magnesium alloy significantly improved corrosion resistance, reducing the corrosion current density (j_{corr}) from 43.52 μA/cm² to 0.351 μA/cm² [57]. In the phosphate system, $Mg_3(PO_4)_2$ (farringtonite) was generated, but the higher porosity of the coating resulted in inferior corrosion resistance compared to the silicate system [58–60].

Durdu et al. [61] investigated the hardness and wear resistance of MAO coatings on magnesium alloys. Figure 8a shows the coatings prepared in silicate-based electrolytes exhibited significantly higher hardness (260–470 HV) compared to those formed in phosphate-based electrolytes (175–260 HV). Regarding adhesion strength, the critical load (L_c) of silicate coatings reached 83 N, while phosphate coatings (72–85 N), with optimal adhesion achieved under high current density (0.14 A/cm²), see the Figures 8b and 8c. While the wear resistance improved by 2–3 times (wear rate as low as 5.6×10^{-5} mm³/N·m for the current density is 0.140 A/cm²), as illustrated in Figure 8d. However, MAO coatings synthesized in aluminate-based electrolytes demonstrated inferior wear resistance performance on AZ91 magnesium alloy [60].

 doi:10.20944/preprints202509.1363.v1

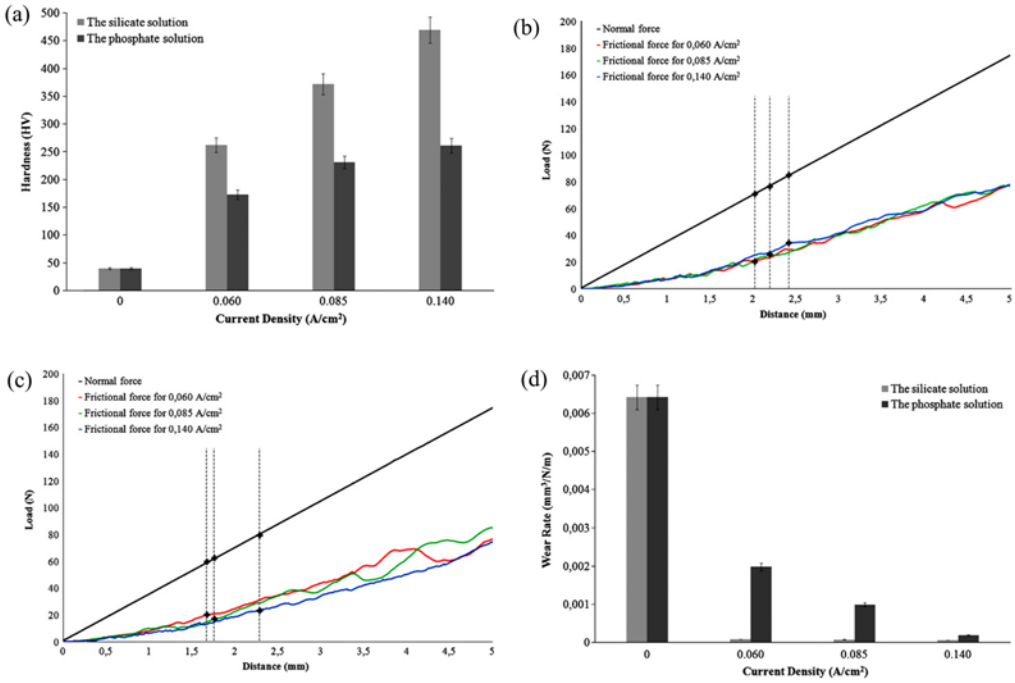

Figure 8. Characterization and mechanical properties of coatings on magnesium by micro arc oxidation. (a) Average hardness of pure magnesium and the micro arc oxide coatings produced different current densities for 30 min: Light gray: the silicate solution and dark gray: the phosphate solution; (b) Load–distance curve for the coatings produced in the silicate solution; (c) Load–distance curve for the coatings produced in the phosphate solution; (d) Wear rates of commercial pure magnesium and the micro arc oxide coatings produced at different current densities during 30 min: Light gray: the silicate solution and dark gray: the phosphate solution. [61].

The ceramic coatings formed on magnesium alloys via MAO technology exhibit excellent biocompatibility. ZK60 magnesium alloy was used to prepare ceramic coatings through MAO in electrolytes containing calcium (Ca) and phosphorus (P) with Ca/P ratios of 1:1, 3:1, and 5:1. After 30 days of immersion in simulated body fluid (SBF), hydroxyapatite (HA) and calcium pyrophosphate (CPP) formed on the coating surface. In vitro cytotoxicity tests (MTT assay) demonstrated a cell survival rate exceeding 95% [62]. Research by Pan et al. [63] on calcium phosphate coatings prepared via MAO on ZK60 magnesium alloy revealed that higher-concentration electrolytes (0.010 mol/L Ca/P) promoted the formation of more HA and CPP on the coating surface, which is shown in Figure 9. XRD patterns of CaP coatings in two electrolytes are shown in Figure 9a, coatings primarily contain MgO, MgF_2, ZnF_2, CaO, CaF_2, and β-$Ca_3(PO_4)_2$ despite varying Ca/P concentrations, with no HA detected. Porous and thin coatings result in strong substrate Mg peaks. β-$Ca_3(PO_4)_2$ confirms P incorporation; this phase is a highly soluble biocompatible ceramic. Compared with pre-immersion XRD (Figure 9a), substrate Mg diffraction peaks weakened, indicating coating coverage by a new layer post-SBF immersion. XRD analysis (see the Figure 9b) revealed HA, $Ca_2P_2O_7$, $Mg(OH)_2$ and $Mg_3(PO_4)_2$ formation with β-$Ca_3(PO_4)_2$ dissolution (due to high solubility in SBF). HA exhibits non-toxicity, bone-bonding ability, and is ideal for hard tissue implants [63].

 doi:10.20944/preprints202509.1363.v1

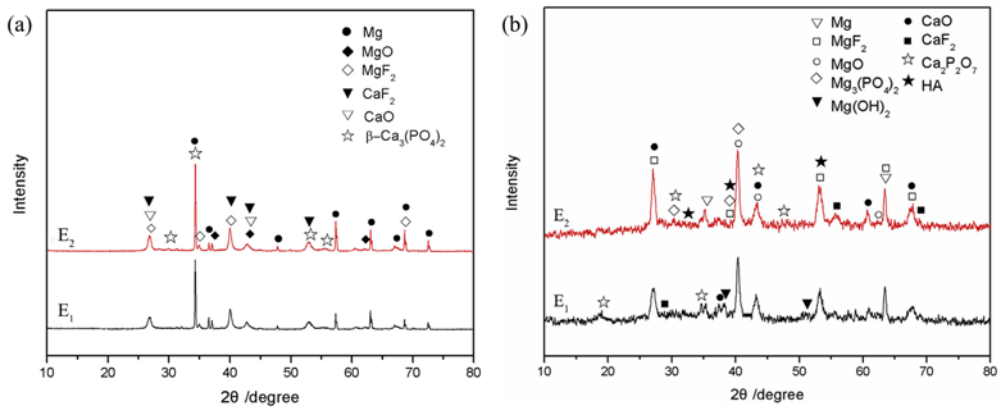

Figure 9. XRD patterns of (a) CaP coatings formed in electrolyte E_1 and electrolyte E_2, (b) CaP coatings after immersion in 1.0 SBF for 30 days. E_1: 0.005 mol /L ($(CH_3COO)_2Ca+Na_2HPO_4$), E_2: 0.010 mol /L($(CH_3COO)_2Ca+Na_2HPO_4$) [63].

In vivo experiments (rabbit femoral implantation), MAO-coated samples showed no abnormalities in serum biochemical indicators such as magnesium, creatinine, and blood urea nitrogen (BUN). Micro-CT imaging indicated greater new bone formation around MAO-coated samples compared to uncoated ones [64]. Studies on the degradation mechanism of MAO coatings on magnesium alloys found that degradation rates correlate with protein type and concentration. In protein-rich physiological environments (e.g., plasma), the degradation behavior of coatings differs from that in pure SBF. Proteins like albumin accelerate localized corrosion by chelating Mg^{2+}, yet they facilitate the long-term formation of protective HA layers [65].

Shao et al. [66] addressed the insufficient corrosion resistance of MAO films on magnesium AZ31 alloys in physiological environments by proposing surface structure and performance optimization through high-intensity pulsed ion beam (HIPIB) irradiation. Combining thermodynamic numerical simulations with experimental validation, the study systematically investigated the influence mechanisms of HIPIB irradiation energy density (1–5 J/cm²) on the microstructure and corrosion resistance of MAO films. Figure 10 illustrates the centrosymmetric surface temperature field of irradiated MAO films, with concentric isotherms and decreasing temperature from the beam spot center; maximum temperature rises with energy density, reaching MgO's boiling point (3873 K) at 4–5 J/cm², while melting/ablation radii increase from 3.2/1.1 mm (4 J/cm²) to 5.5/1.4 mm (5 J/cm²). The work revealed that HIPIB irradiation optimizes MAO film structure through temperature-stress coupling effects, establishing a synergistic model of "densified layer formation, grain refinement, and hydrophobic modification" to enhance corrosion resistance. This research provides an efficient and controllable surface modification strategy for magnesium alloys, particularly applicable to corrosion resistance enhancement in biodegradable implants (e.g., orthopedic fixation devices), while offering theoretical foundations for industrial anti-corrosion coating development [66].

 doi:10.20944/preprints202509.1363.v1

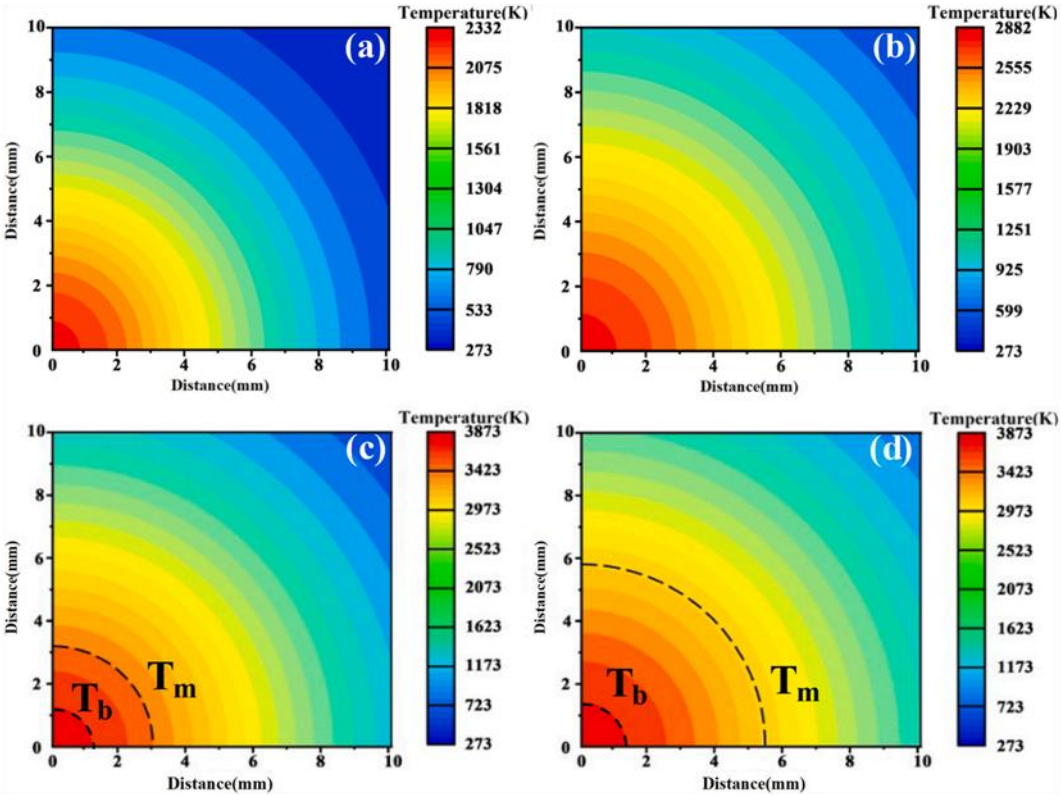

Figure 10. The surface temperature field distribution of irradiated MAO films by HIPIB at 1–5 J/cm². (a) 1 J/cm², (b) 2 J/cm², (c) 4 J/cm², (d) 5 J/cm² [66].

2.3. MAO Treatment Technology for Ti-Based Alloys

Titanium and its alloys are widely utilized in biomedical fields such as orthopedic implants and dental prostheses due to their excellent mechanical properties, corrosion resistance, and biocompatibility [67–69]. However, the inherent bioinertness of titanium alloy surfaces limits their direct bonding ability with surrounding bone tissue, and corrosion behavior in physiological environments may lead to metal ion release, triggering long-term implant failure risks. MAO treatment of titanium-based alloys is a surface modification technique developed from anodic oxidation, which triggers micro-arc discharge via applying high voltage to in-situ grow ceramic oxide films on the alloy surface [70]. The oxide film produced by this technique exhibits strong adhesion to the substrate, high hardness, wear resistance, corrosion resistance, and insulation properties [71–73].

For instance, Han et al. [74,75] systematically investigated the formation mechanism of HA coatings under calcium-phosphate electrolyte systems, revealing the regulatory effect of high voltage (> 450 V) induced melting-recrystallization on coating densification. The processing parameters of the micro-arc oxidized samples are shown in Table 3 [75]. To further optimize performance, researchers have introduced functional additives: Song et al. [76] endowed coatings with long-term antibacterial activity (bacterial inhibition rate > 95% against Staphylococcus aureus) by doping with Ag or Cu ions; the incorporation of ZrO_2 particles enhanced coating hardness to over 12 GPa via dispersion strengthening, significantly improving wear resistance [77]. Additionally, studies on the synergistic effect of MAO with ultrafine grained titanium substrates demonstrated that nanostructured substrates can accelerate coating growth and enhance interfacial bonding strength (> 50 MPa), providing new insights for the design of drug-loaded sustained-release coatings [78,79].

Table 3. Processing parameters of the micro-arc oxidized samples [75].

Sample	Electrolyte composition	Applied voltage (V)	Initial current density (mA·mm^{-2})	Final current density (mA·mm^{-2})
A1	0.6 M Na_2CO_3	200	4.69	0.63

 doi:10.20944/preprints202509.1363.v1

A2	0.6 M Na_2CO_3	350	8.78	1.53
B1	0.2 M CA	350	7.34	1.4
B2	0.2 M CA	400	9.69	2.13
C1	0.04 M Na_3PO_4	350	2.18	0.16
C2	0.04 M Na_3PO_4	450	4.28	1.09
D1	0.2 M CA + 0.02M β-GP	250	2.09	0.06
D2	0.2 M CA + 0.02M β-GP	350	4.53	0.12
D3	0.2 M CA + 0.02M β-GP	450	7.03	0.47
D4	0.2 M CA + 0.02M β-GP	500	9.53	0.66

MAO, as an efficient surface modification technique, significantly enhances the bioactivity, corrosion resistance, and functional performance of titanium and its alloys by in-situ forming porous ceramic coatings. Below is a summary of key findings and technological advancements from multiple related studies.

Nanocrystalline anatase TiO_2 coatings prepared by MAO [80], when subjected to UV irradiation, generate abundant Ti^{3+} and oxygen vacancies on the surface. The MAO coating remained porous without precipitate after 25-day SBF immersion, showing no bonelike apatite induction. UV-0.5 h coatings developed sphere-like particles at 17 days (full surface coverage by 19 days) but none at 15 days shows in Figure 11a. UV-2 h coatings exhibited such particles as early as 13 days, with a dense precipitate layer fully covering the surface by 17 days, as Figure 11b shows. Figure 11c shows the surface morphology and XRD pattern of the dark-stored UV-2h coating after 17-day SBF immersion, indicating apatite induction within a short SBF immersion period. XPS analysis and further reveal the UV-irradiated coating exhibits long-term stability of Ti-OH groups and sustained bioactivity. Figure 11d shows ALP activity of cells cultured on MAO and UV-2 h coatings over 1-3 days: no statistical difference before day 2, but UV-2 h coatings exhibited significantly higher ALP activity than MAO coatings at day 3.

Kung et al [81] studied the MAO coatings on titanium substrates, which were prepared in Sr-containing calcium-phosphate electrolytes, that exhibit a porous structure incorporating Sr, Ca, and P. Apatite formation initiates after 1 day of SBF immersion and fully covers the surface within 7 days. The release of Sr ions promotes bone formation. Electrochemical tests reveal that these coatings display a more noble corrosion potential (E_{corr}) and lower passive current density compared to pure titanium, indicating superior corrosion resistance. Biological response of Ti6Al4V and Ti6Al7Nb alloys [82], after MAO treatment, forms ~10 μm thick TiO_2 coatings (anatase + rutile). The Ti6Al4V coating is more porous and contains HA, whereas the Ti6Al7Nb coating exhibits a granular structure with calcium titanate ($CaTiO_3$). Both coatings induce apatite formation in SBF. Cell experiments show that the Ti6Al4V oxide layer, due to its more microporous structure, supports better SAOS-2 cell adhesion than the Ti6Al7Nb coating [82].

 doi:10.20944/preprints202509.1363.v1

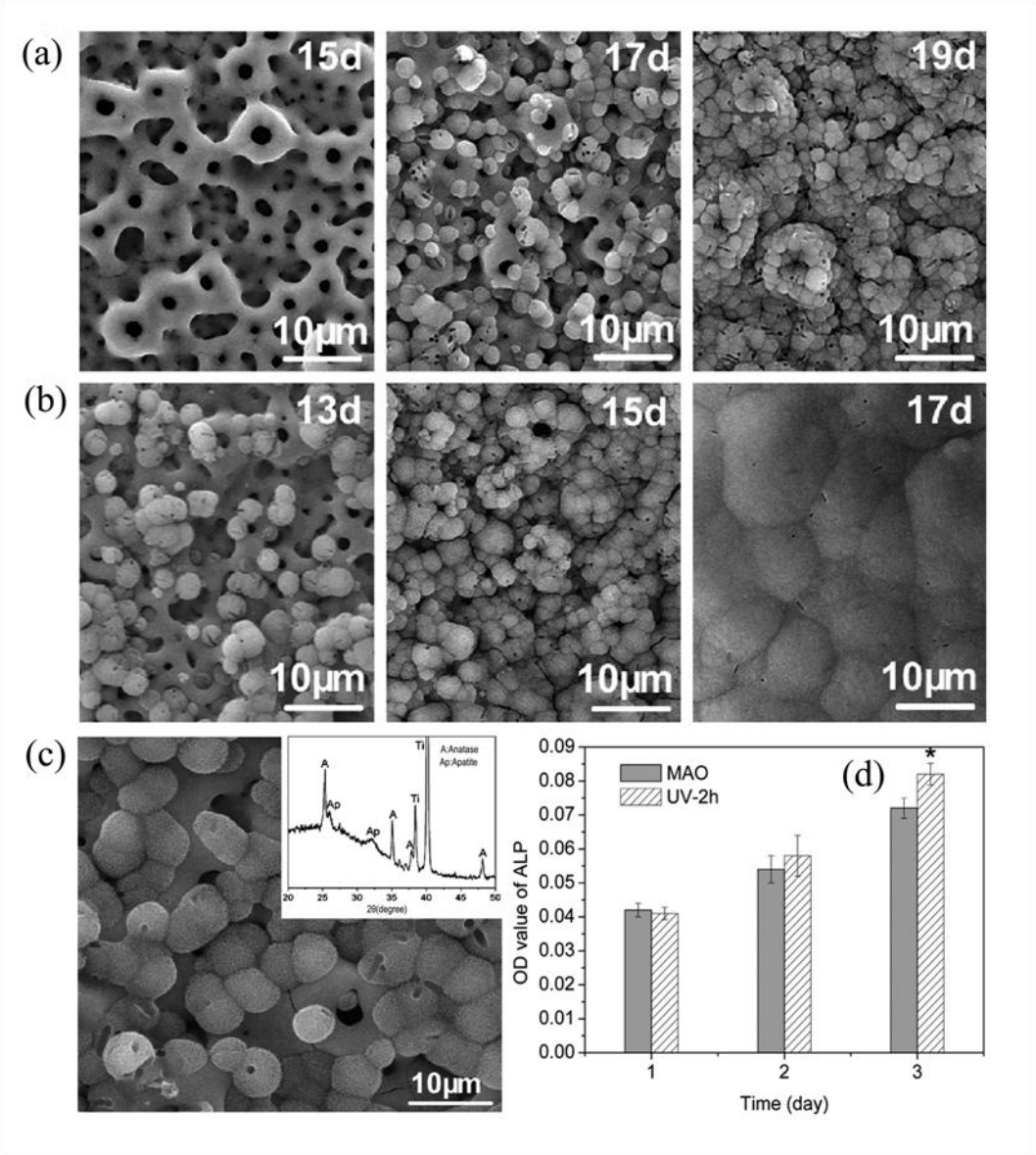

Figure 11. UV-enhanced bioactivity and cell response of micro-arc oxidized titania coatings. Surface morphologies of (a) the UV-0.5 h and (b) the UV-2 h coatings after immersion in SBF for different times (notes in the pictures); (c) SEM view and XRD spectrum of the dark-stored UV-2 h coating after immersion in SBF for 17 days; (d) Alkaline phosphatase activities of the cells cultured on the MAO and UV-2 h coatings for 1, 2 and 3 days. * Significant at $P < 0.05$, UV-2 h coating *vs*. MAO coating [80].

Li et al [83] researched the MAO treatment that forms a porous and dense oxide layer on titanium surfaces, XRD analysis (Figure 12A) characterized the phases of oxide layers: MAO-prepared layers consisted of rutile and Ti, while sandblasted surfaces contained anatase and Ti. Compared to sandblasted surfaces, MAO-treated surfaces exhibit a smaller contact angle (55.4° *vs*. 74.4°) as revealed in the Figure 12B. The titanium-porcelain bond strength increases from 33.28 MPa to 46.46 MPa (39.6% improvement), which is primarily attributed to: 1) the porous structure enhancing mechanical interlocking; 2) the stable rutile phase inhibiting high-temperature oxidation; 3) improved hydrophilicity promoting porcelain wetting. For TC4 alloys fabricated by selective laser melting (SLM), the growth characteristics (e.g., thickness, porosity) of MAO coatings are dependent on oxidation time.

 doi:10.20944/preprints202509.1363.v1

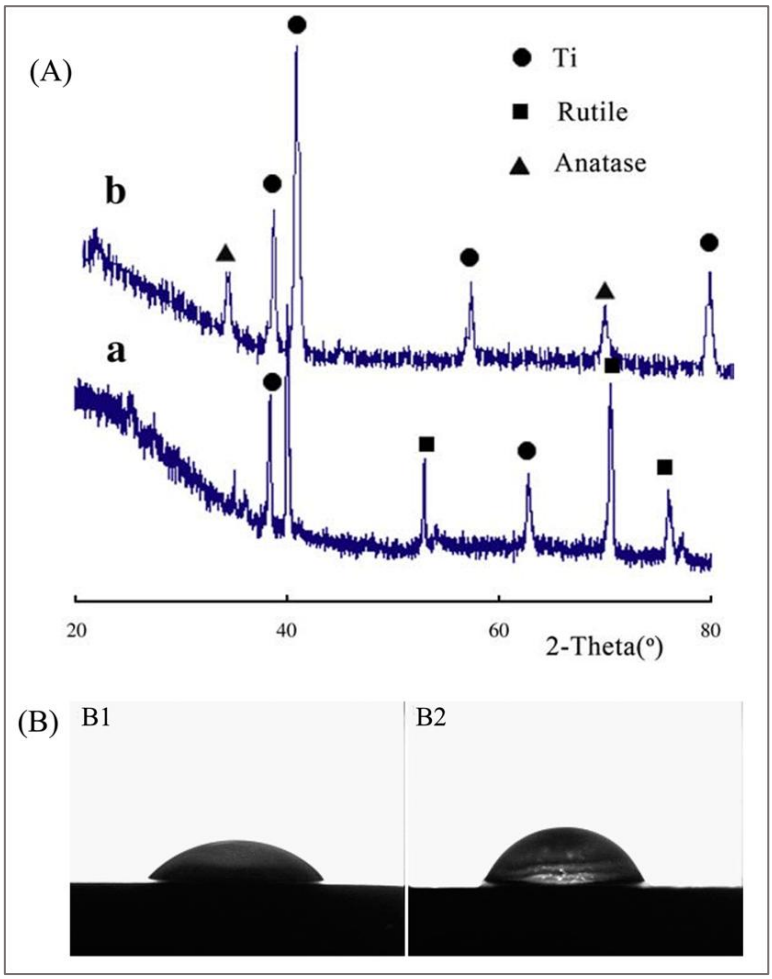

Figure 12. Effects of micro-arc oxidation on bond strength of titanium to porcelain. (A) XRD patterns of MAO-treated and sandblasting Ti surfaces: (a) MAO treatment and (b) sandblasting treatment; (B) Contact angles of water: (B1) MAO treatment; and (B2) sandblasting treatment [83].

Optimized coatings exhibit both bioactivity and mechanical stability as reported by Yao et al. [84]. Figure 13a presents the adhesion of MAO coatings at different oxidation times and their scratch micrographs. The adhesion first increased from 15.22 N (5 min) to 20.86 N (15 min), then decreased to 17.73 N (20 min), indicating oxidation time influences adhesion strength with an optimal range. Figure 13b1 shows the potentiodynamic polarization curves (36.5 °C SBF solution) for MAO coatings (varied oxidation times) and substrate. MAO coatings exhibited lower I_{corr} than substrate, confirming effective corrosion protection for SLM-TC4 alloy. I_{corr} decreased with oxidation time up to 15 min, then increased at 20 min despite higher thickness. The 15 min coating showed optimal performance: ~1 order lower I_{corr} and 444 mV positive E_{corr} shift versus substrate. Bode plots (Figure 13b2) revealed higher low frequency (LF) impedance modulus for all MAO coatings compared to substrate, with 15 min coatings showing maximum LF/HF impedance (indicating enhanced inner compact/outer porous layer resistance). Impedance decreased at 20 min, consistent with polarization results. Figure 13 c outlines the four-stage MAO process for Ca-P-containing titania coatings on SLM-TC4 alloy: Stage I: Initial anodic oxidation forms a primary layer; voltage rises to breakdown, triggering spark discharge and channel formation, transitioning to puncturing; Stage II: Spark discharge propagates with stable channels, enabling localized oxide melting and coating nucleation; Stage III: Under constant current, coating grows steadily (thickness/impedance increase); rough porosity aids apatite nucleation, with Ca/P incorporation and phase evolution enhancing properties; Stage IV: Prolonged oxidation increases porosity/defects, reducing compactness; SBF penetration and reduced surface Ca/P decrease corrosion resistance and bioactivity.

 doi:10.20944/preprints202509.1363.v1

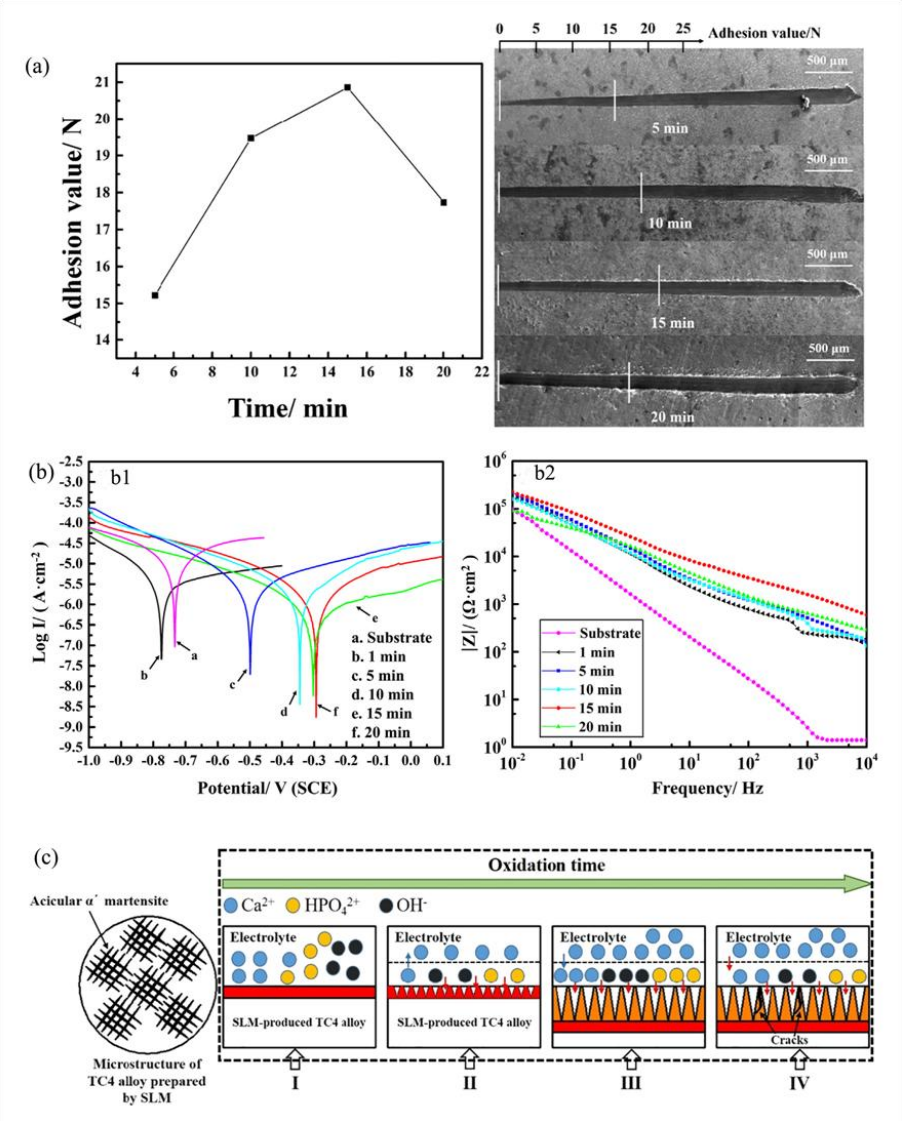

Figure 13. Growth characteristics and properties of micro-arc oxidation coating on SLM-produced TC4 alloy for biomedical applications. (a) The adhesion value (left) and scratch morphologies (right) of the MAO coatings produced at difference oxidation times; (b) Plots of the substrate and MAO coatings in different oxidation times in SBFs' solution, (b_1) Potentiodynamic polarization curves and (b_2) experimental Bode; (c) Schematic diagram of MAO process on SLM-produced TC4 alloy [84].

Ceramic coatings prepared by MAO in aluminate electrolytes on titanium alloys form dense Al-Ti-O composite oxide layers, significantly enhancing the high temperature oxidation resistance by inhibiting oxygen diffusion into the substrate [85]. Meanwhile, MAO can also enhance the high-temperature oxidation resistance of additively manufactured Ti2AlNb alloys [86].

Micro-arc oxidation technology, through the regulation of electrolyte composition, electrical parameters, and post-treatments, enables the construction of multifunctional coatings on titanium and its alloys: (1) Bioactivity: Induces bone-like apatite formation and promotes osseointegration; (2) Corrosion Resistance: Reduces corrosion current and enhances long-term stability; (3) Functional integration: Promotes bone formation via strontium-containing coatings, regulates hydrophilicity through UV irradiation, and provides high-temperature oxidation protection.

2.4. MAO Treatment Technology for High-Entropy Alloys

High-entropy alloys (HEAs), particularly refractory high-entropy alloys (RHEAs), are considered candidates for next-generation high-temperature structural materials due to their

 doi:10.20944/preprints202509.1363.v1

excellent high-temperature mechanical properties (e.g., high strength and resistance to softening) [87–89]. However, RHEAs often contain volatile elements such as V, Mo, and W, whose high-temperature oxidation products (e.g., V_2O_5, MoO_3) are prone to volatilization or form loose oxide films, leading to poor high-temperature oxidation resistance and limiting their practical applications. MAO, also known as an environmentally friendly and efficient surface treatment technology, has emerged as a critical method to enhance the high-temperature oxidation resistance of RHEAs by in-situ growing ceramic coatings [90]. The development is summarized below from the perspectives of background, process optimization, coating characteristics, performance enhancement, challenges, and future directions.

RHEAs are composed of refractory elements such as Ti, V, Cr, Zr, Nb, and Mo, and maintain high strength even above 1000°C (e.g., the yield strength of NbMoTaW exceeds 400 MPa at 1600°C). However, their high-temperature oxidation often results in volatile oxides (e.g., V_2O_5, MoO_3) or loose oxide films (e.g., Nb_2O_5), causing significant mass gain and protective failure [91–93]. For instance, the oxidation layer thickness of $AlTiNbVZr_{0.25}$ can reach 800 μm due to V volatilization at high temperatures [94]; the mass gain of uncoated $AlTiNbMo_{0.5}Ta_{0.5}Zr$ reaches 12.91 mg/cm² [91]. MAO forms ceramic coatings on alloy surfaces via arc discharge, with strong adhesion to the substrate and controllable composition. It effectively blocks O_2 diffusion and suppresses the oxidation of volatile elements, making it a key technology to address the high-temperature oxidation issues of RHEAs [95–97].

MAO process parameters (e.g., electrolyte composition, voltage) directly affect coating quality. Key optimization directions include: (1) Electrolyte composition optimization. Basic electrolytes often use silicon- and phosphorus-containing solutions (e.g., Na_2SiO_3, $(NaPO_3)_6$) to promote the formation of stable oxides such as SiO_2 and phosphates, enhancing coating stability [91,94]. Additives like $Na_2B_4O_7$ and KF can suppress uneven discharge and reduce microcracks and pores. The corresponding micro-arc oxidation electrolyte compositions and process parameters are shown in Table 4.

Table 4. Processing parameters of the micro-arc oxidized HEAs [91,94].

References	Electrolyte Composition	Process Parameters
Ref 91	Na_2SiO_3 (12 g/L) + NaOH (1.2 g/L)	Voltage: 500 V, Frequency: 500 Hz, Duty cycle: 10%, Time: 10 min
Ref 94	Na_2SiO_3 (50 g/L) Na_2SiO_3 (50 g/L) + $(NaPO_3)_6$ (25 g/L) + NaOH (5 g/L) Na_2SiO_3 (50 g/L) + $(NaPO_3)_6$ (25 g/L) + NaOH (5 g/L) + $Na_2B_4O_7$ (3 g/L) + KF (4 g/L)	Voltage: 450 V, Frequency: 600 Hz, Duty cycle: 8%, Time: 5 min

For example, Shi et al. [94] found that adding $Na_2B_4O_7$ and KF to Na_2SiO_3+$(NaPO_3)_6$+NaOH reduced the surface roughness of AlTiCrVZr MAO coatings from 16.507 μm to 7.241 μm, decreased V content (inhibiting V_2O_5 volatilization), and improved coating densification. (2) Voltage parameter regulation. Voltage influences coating thickness and densification. Figure 14A shows the surface morphology and EDS results of MAO coatings under different electrolytes. All coatings exhibit a porous "crater" morphology with microcracks: (a1) Na_2SiO_3 electrolyte results in rough, porous coatings with microcracks and particle aggregation, dominated by Si/O; (b1) Na_2SiO_3 + $(NaPO_3)_6$ + NaOH yields smoother, denser coatings with fewer cracks; (c1) Adding $Na_2B_4O_7$ + KF produces dense coatings with uniform micropores and reduced cracks. Figure 14B presents cross-sectional morphologies and EDS results of MAO coatings formed in three electrolytes. All coatings are thick with good substrate adhesion but show local overgrowth. (1) Na_2SiO_3 electrolyte: about 60 μm thickness, numerous micropores and obvious cracks; EDS reveals dominant Si/O, with Al/O

 doi:10.20944/preprints202509.1363.v1

enrichment at the outer coating; (2) Na_2SiO_3 + $(NaPO_3)_6$ + NaOH: approximately 40 μm thickness, no obvious pores/cracks; EDS indicates O/Si/Al/Zr/P as main elements, with elevated Al at the coating-substrate interface and increased Cr content; (3) Na_2SiO_3 + $(NaPO_3)_6$ + NaOH + $Na_2B_4O_7$ + KF: around 30 μm thickness, densest cross-section among the three.

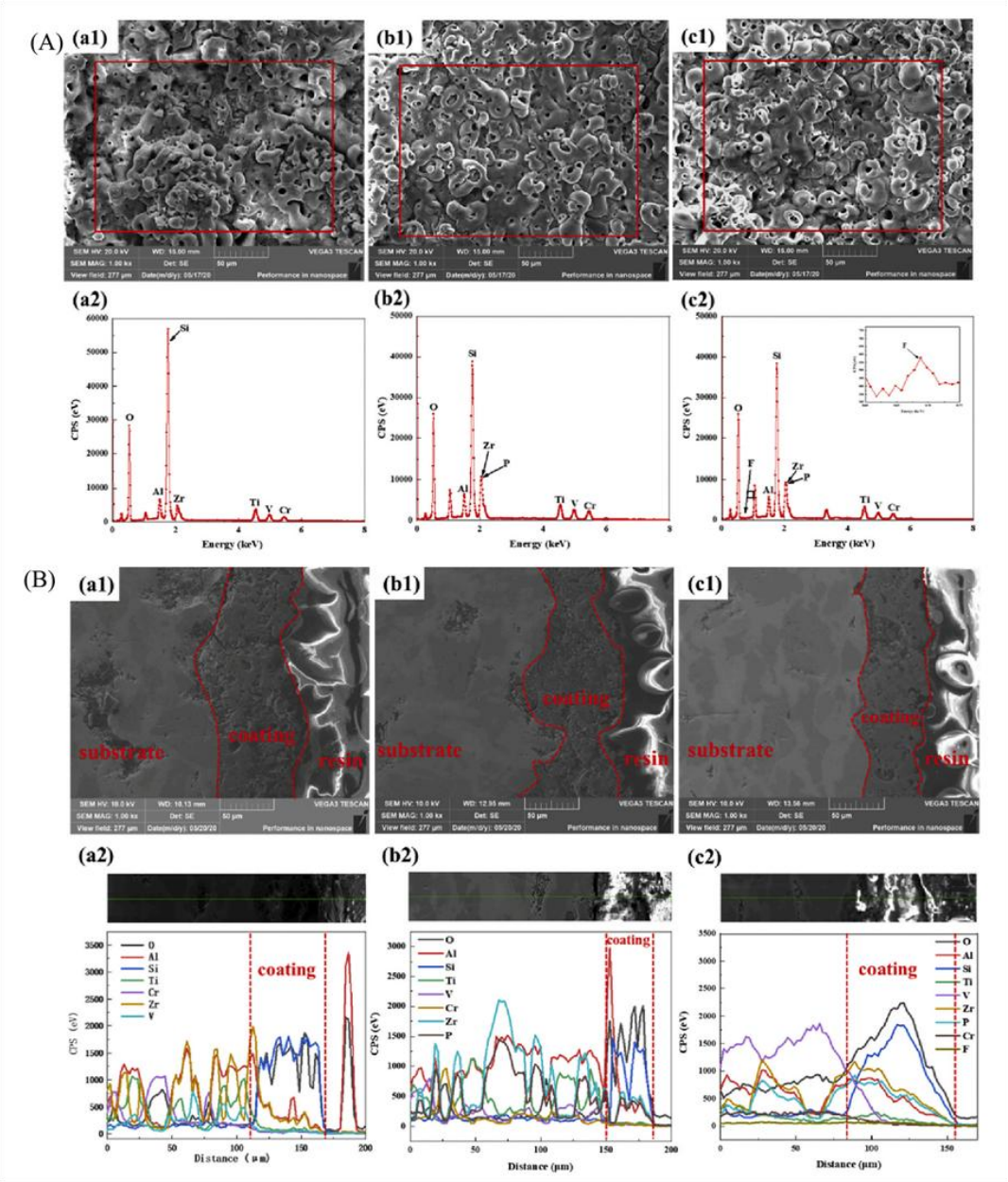

Figure 14. Influence of micro arc oxidation on high temperature oxidation resistance of AlTiCrVZr refractory high entropy alloy. (A) Surface morphology and EDS and (B) Cross-sectional morphologies of MAO coatings in different electrolytes: (a) Na_2SiO_3, (b) Na_2SiO_3 + $(NaPO_3)_6$ + NaOH, (c) Na_2SiO_3 + $(NaPO_3)_6$ + NaOH + $Na_2B_4O_7$ + KF [94].

Wang et al. [95] studied MAO coatings on AlTiCrVZr and found that increasing voltage from 360 V to 450 V increased coating thickness from 40 μm to 50 μm, as presented in the Figure 15a–d. However, excessively high voltage (e.g., 450 V) caused more cracks due to increased thermal stress. The optimal voltage (e.g., 420 V) balanced thickness and densification, the XPS results of 420 V confirms coating elemental compositions (Figure 15e), while showing the best performance after long-term oxidation [95].

 doi:10.20944/preprints202509.1363.v1

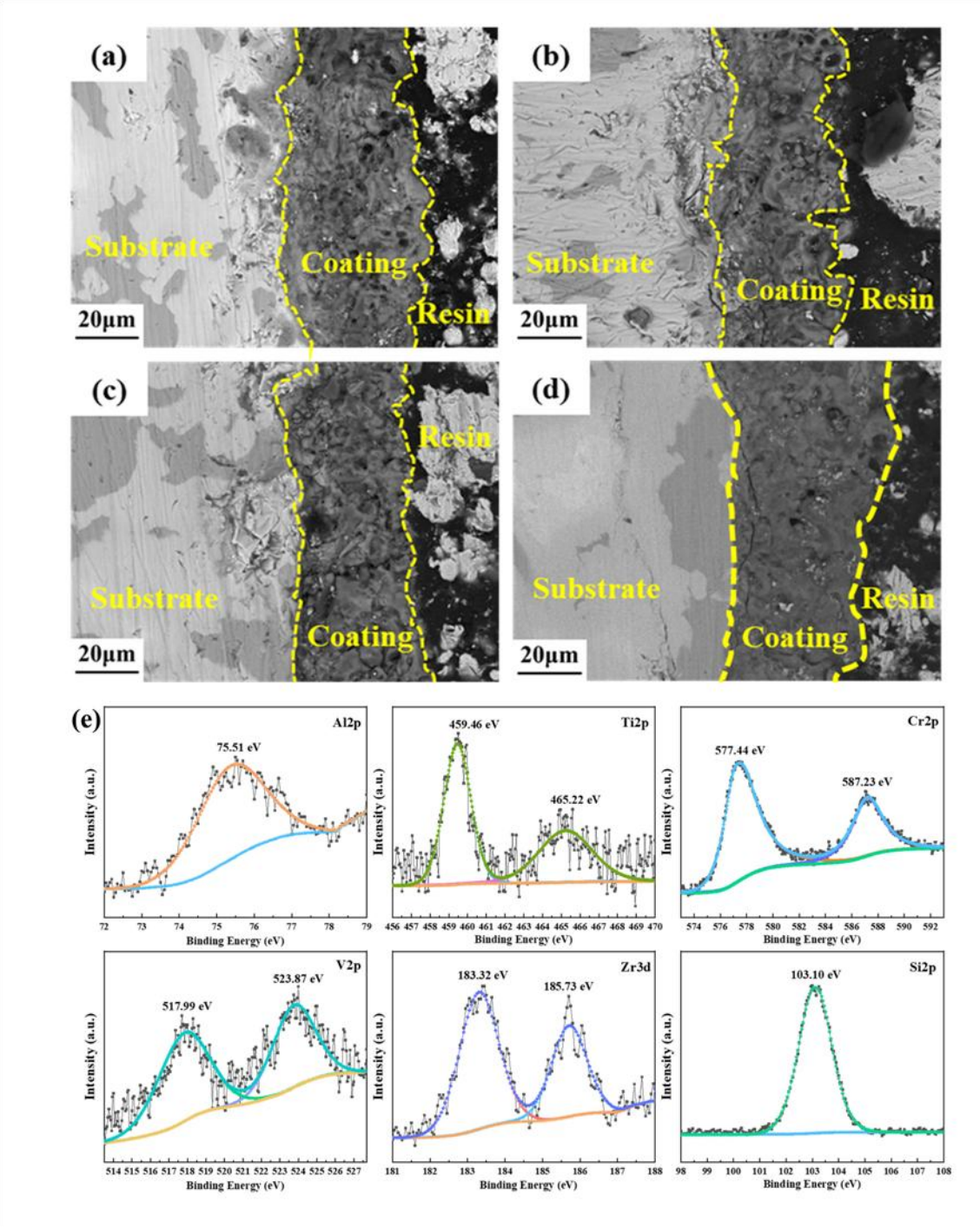

Figure 15. Effect of voltage on the microstructure and high-temperature oxidation resistance of micro-arc oxidation coatings on AlTiCrVZr refractory high-entropy alloy. Cross-sectional morphologies of coatings prepared using different voltages: (a) 360 V, (b) 390 V, (c) 420 V, and (d) 450 V, (e) High-resolution spectrum of each element of the coating prepared at 420 V [95].

The core advantage of MAO coatings lies in their composite protective layers composed of multiple high-temperature stable oxides: (1) Composition: Coatings primarily contain oxides such as Al_2O_3, Cr_2O_3, SiO_2, ZrO_2, and TiO_2 (confirmed by XPS analysis), with trace V_2O_5 (content controlled by electrolytes) [91,94,95]. For example, MAO coatings on $AlTiNbMo_{0.5}Ta_{0.5}Zr$ are dominated by SiO_2 and Ta_2O_5 [91], those on AlTiCrVZr contain Al_2O_3, Cr_2O_3 and SiO_2 [94]. (2) Microstructure: Typical "volcanic crater" morphology with micropores (residual discharge channels) and minor microcracks. Optimized coatings (e.g., with $Na_2B_4O_7$ + KF or 420 V voltage) exhibit significantly improved densification, reduced porosity, and tighter interfacial bonding [94,95].

 doi:10.20944/preprints202509.1363.v1

MAO coatings enhance RHEAs' high-temperature oxidation resistance through dual mechanisms: (1) Physical Barrier: Dense coatings directly block O_2 contact with the substrate and inhibit O diffusion. For example, the diffusion layer thickness of uncoated AlTiCrVZr is 800 μm, which decreases to below 600 μm after MAO treatment [60]; the mass gain of $AlTiNbMo_{0.5}Ta_{0.5}Zr$ is reduced from 12.91 mg/cm² to 8.67 mg/cm² with MAO [91]. (2) Chemical Inhibition: Oxides such as Al_2O_3 and Cr_2O_3 in coatings suppress the oxidation and volatilization of volatile elements (e.g., V, Mo). For instance, in $Al_xCoCrFeMnNi$ alloys, increasing Al content leads to the formation of a dense Cr_2O_3/Al_2O_3 film at the coating bottom, reducing oxidation rate and oxide layer thickness [93]. Additionally, MAO coatings can synergistically improve wear and corrosion resistance. For example, the hardness of $Al_xCoCrFeMnNi$ coatings increases with Al content (from 154.5 HV to 631.1 HV), but excessive Al ($x \geq 1.0$) reduces corrosion resistance due to increased BCC phase [93].

2.5. MAO Treatment Technology for Steel

MAO is a technique that uses plasma discharge to in-situ grow ceramic coatings on valve metals (e.g., Al, Mg, Ti). However, steel, as a non-valve metal (without self-passivation properties), cannot directly undergo MAO. In recent years, researchers have constructed composite structures of "interlayer + MAO ceramic layer" on steel surfaces by combining pretreatment techniques (e.g., high-energy micro-arc alloying, wire arc spraying, hot-dip aluminizing, laser cladding), significantly enhancing the high-temperature oxidation resistance, corrosion resistance, wear resistance, and mechanical properties of steel [96].

The core of MAO on steel lies in constructing an interlayer suitable for MAO (e.g., Al-based alloy layers, FeAl or $LaCrO_3$ functional layers) through pretreatment. Methods are categorized into indirect (pretreatment + MAO) and direct (direct MAO) approaches:

(1) Pretreatment + MAO composite processes. Pretreatments form valve metal (e.g., Al, Mg, Ti) or functional alloy layers on steel, followed by MAO. This is the mainstream technique for MAO on steel. 1) High-energy micro-arc alloying (HEMAA) coatings [97–99], a short-pulse high-current micro-welding technique, form dense coatings via metallurgical bonding between electrode materials and substrates, suitable for high-temperature functional coatings (e.g., solid oxide fuel cell (SOFC) interconnects). On ferritic stainless steel (430 SS), a Cr-alloyed layer is first deposited by HEMAA (to enhance adhesion) [97,98], followed by a $LaCrO_3$-20 wt.% Ni electrode, forming a three-layer structure: "$NiFe_2O_4$ outer layer + $LaCrO_3$ middle layer + Cr_2O_3 inner layer." On 316 stainless steel, a 50μm-thick FeAl coating (38.26 at.% Al) is prepared by HEMAA [99], with significantly refined grains (electrode grains: 50-150 μm; coating grains: finer). 2) Wire arc spraying + MAO composite process [11]. Al-based alloy layers (Al-Mg6, Al-Si 12, or pure Al) are first deposited on low-carbon steel (AISI 1010) by wire arc spraying, followed by MAO. Spraying parameters (current: 100-300 A; voltage: 28-32 V; distance: 15-20 cm; pressure: 3-4 Bar) affect coating thickness. MAO converts Al-based layers into Al_2O_3-based ceramic layers [11]. 3) Hot-dip aluminizing + MAO. Low-carbon steel (Q235) [100] or high-strength steel (AerMet100) [101] is hot-dip aluminized (710°C, 2 min) to form a "Fe-Al alloy layer + pure Al layer" structure, followed by MAO. The MAO process includes three stages: common anodization (thin oxide film), stable micro-arc oxidation (ceramic layer growth), and coating destruction (outer layer ablation by large arcs). Current density (0.5-2.5 A/dm²) and time (0-14 min) affect total ceramic thickness (max ~47.5μm) and inner/outer layer ratio (higher current promotes outer layer growth). 4) Laser cladding + MAO [12]. Al-based alloy layers (e.g., Al-Si) are first laser-clad on S355 offshore steel, followed by MAO. Laser cladding adjusts interlayer composition and density, resulting in Al_2O_3-based ceramic layers with higher adhesion strength (>50MPa) than wire arc spraying + MAO (~30 MPa) [12]. 5) Electro-spark deposition (ESD) + MAO [103]. Al- or Ti-based alloy layers (5-10 μm thick) are first deposited on steel by ESD, followed by MAO. ESD enables precise interlayer composition control, forming α-Al_2O_3 or TiO_2 containing ceramic layers suitable for bioactive coatings on medical steel (e.g., Ti-alloyed steel). The composition of electrolytes and electrical parameters for several typical micro arc oxidation treatment methods is shown in Table 5. Figure 16a is the Schematic setup for area-specific contact resistance measurements [97], while Figure

 doi:10.20944/preprints202509.1363.v1

16b to 16d shows schematic diagrams of typical setups for different methods of micro-arc oxidation treatment on steel surfaces [11,101,102].

Table 5. The composition of electrolytes and electrical parameters for several typical micro arc oxidation treatment methods [11,12,100,102].

Different methods	Wire arc spraying + MAO	Hot-dip aluminizing + MAO	Laser cladding + MAO	Electro-spark deposition + MAO
Electrolyte composition	5 g/L $Na_2B_4O_7$, 5 g/L KOH, 2 g/L Na_3PO_4, 20 g/L glycerin, with distilled water as the solvent	8 g/L KOH, 10 g/L Na_2SiO_3, with distilled water as the solvent	12 g/L Na_2SiO_3, 5 g/L KOH, 0.5 g/L NaF, 3 g/L SiO_2, 9 g/L TiO_2	1.65 g/L Na_3PO_4, 8 g/L $NaAlO_2$
Electrical parameter	Current density: 12 A/dm², electrolyte temperature: 20–35°C, processing time: 50–150 min	Current density: 0.5–2.5 A/dm², electrolyte temperature: 40 ± 2°C, processing time: 0–14 min	Current density: 3 – 8 A/dm² (optimal 5 A/dm²), electrolyte temperature: 30°C, processing time: 30 min	Cnode voltage: 550 V, cathode voltage: 160 V, processing time: 30 min

(2) Direct Methods. Direct MAO on steel is attempted via electrolyte optimization (e.g., adding high-activity metal ions) or pretreatment (e.g., passivation layers) [104–106]. 1) Passivation Layer-Assisted MAO [104]: A Cr-based passivation film (1-2 μm thick) is first formed on low-carbon steel, followed by MAO. The self-repairing passivation film suppresses steel dissolution, resulting in Fe_3O_4-Cr_2O_3 composite ceramic layers (~ 20 μm thick). 2) Electrolyte-controlled MAO [105,106]: Using strongly alkaline electrolytes (pH > 13) with Na2SiO3 and KOH, α-Al_2O_3 (Fe-doped) ceramic layers (~ 15 μm thick) are formed on low-carbon steel (10B21) via Fe oxidation-dissolution-redeposition, though with lower density (porosity > 10%), and the composition of electrolytes and electrical parameters are shown in Table 6.

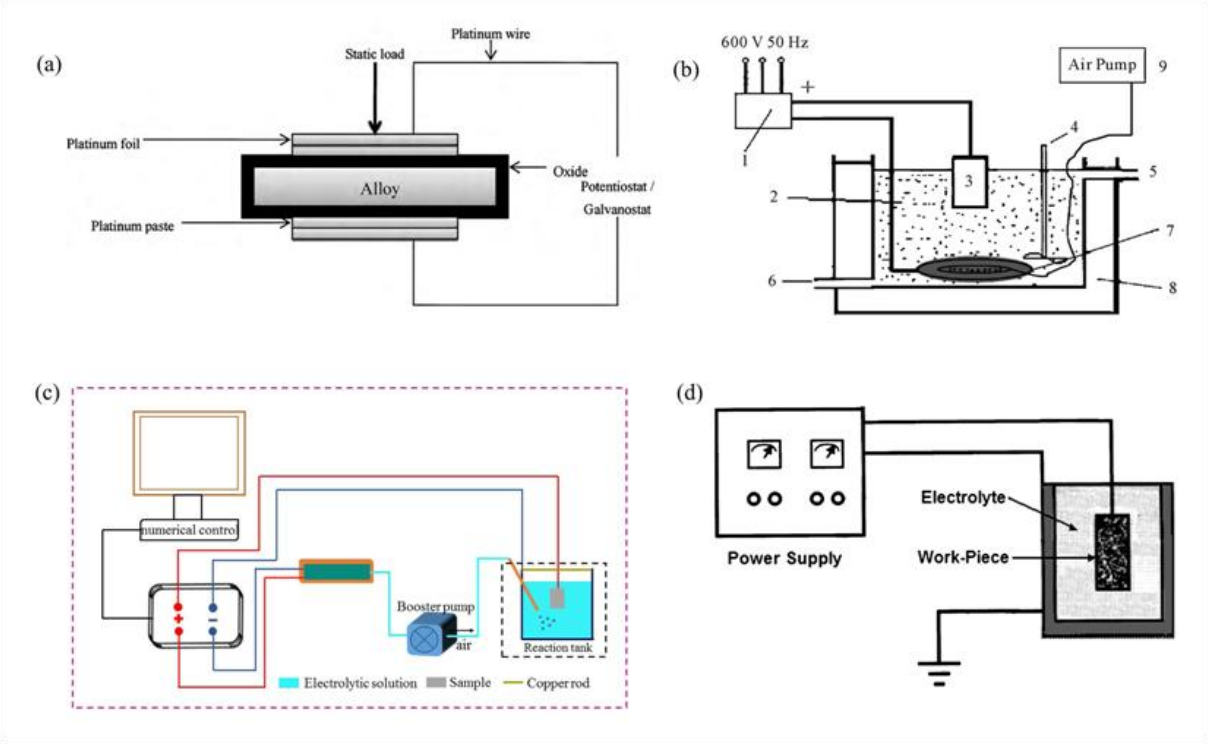

Figure 16. (a) Schematic setup for area-specific contact resistance measurements [97]; (b) Schematic view of micro arc oxidation deposition system on alloy steel: 1: power supply and control system, 2: electrolyte, 3: workpiece,

 doi:10.20944/preprints202509.1363.v1

4: mixer, 5: cooling water inlet, 6: cooling water outlet, 7: stainless-steel anode plate, 8: plexiglass, 9: air pump [11]; (c) Schematic of micro-arc oxidation process on AerMet100 steel [101]; (d) Schematic representation of micro-arc oxidation coating system set up on St35 [102].

Table 6. The composition of electrolytes and electrical parameters of electrolyte-controlled MAO [106].

Coatings	$NaAlO_2$ (g/L)	NaH_2PO_4 (g/L)	Na_2CO_3 (g/L)	$Na_2B_4O_7$ (g/L)
M1	15	3		
M2	15	3	3	
M3	15	3	3	3

Sun et al. [104] illustrate in Figure 17A the preparation steps and mechanism of PASS+MAO coating: low-carbon steel surface undergoes passivation to form a rough passivation layer, followed by MAO treatment. During MAO, alternating current pulse causes micro-arc discharge on the anode, generating localized high temperatures (> 1000°C), vaporizing water to form bubbles as channels for charge transfer and arc discharge, resulting in a composite coating. Li et al.[106] present in Figure 17B the formation mechanism of MAO coatings in three electrolytes. M1 ($NaAlO_2$-NaH_2PO_4) forms Al_2O_3 with Fe_2O_3/$FePO_4$ via arc discharge and Fe oxidation. M2 adds Na_2CO_3, enhancing arc discharge and Al_2O_3 growth. M3 with Na_2CO_3-$Na_2B_4O_7$ inhibits Fe compounds, promotes α-Al_2O_3 via B_2O_3 dissolving Fe_2O_3, forming dense, corrosion resistant coatings.

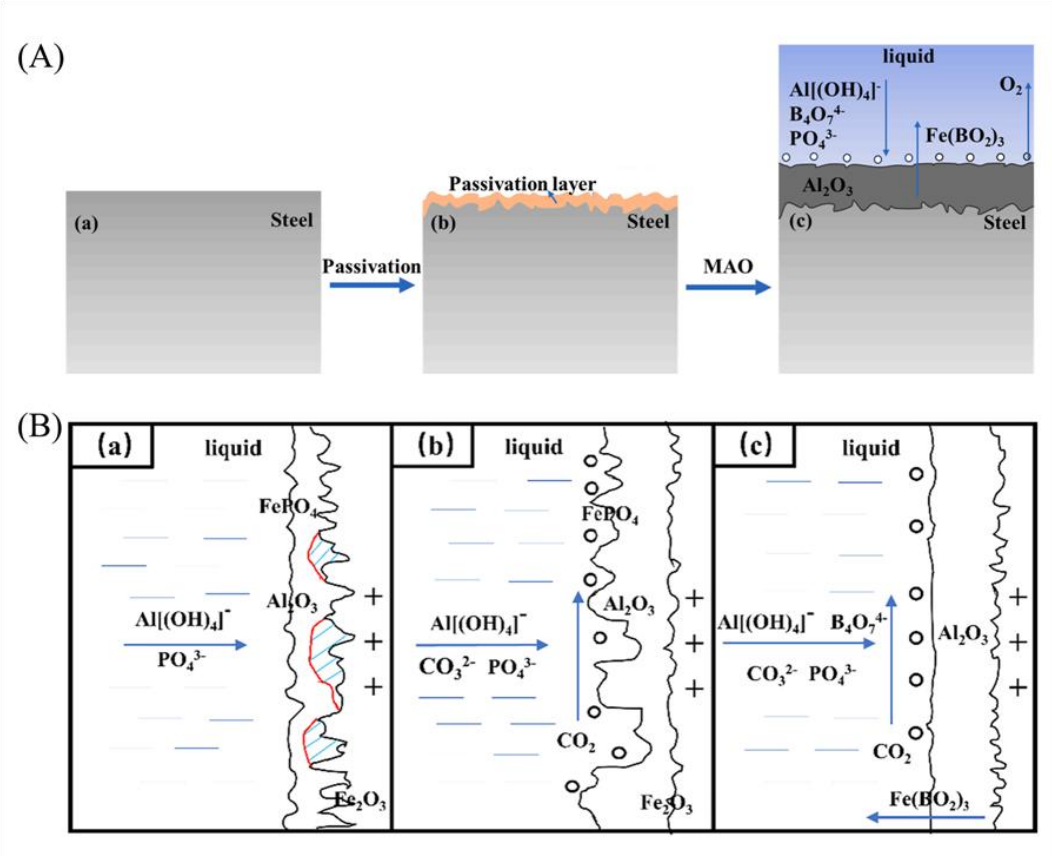

Figure 17. (A) Research on micro-arc oxidation method based on passivation layer on non-valve metal low-carbon steel surface. Flowchart (a), (b) and (c); Mechanism diagram (c) [104]; (B) Preparation, characteristics and corrosion properties of α-Al_2O_3 coatings on 10B21 carbon steel by micro-arc oxidation. Formation mechanism of MAO coatings produced by different electrolytes: (a) M1, (b) M2, (c) M3 [106].

Performance varies significantly among different pretreatment + MAO composite coatings, with a focus on high-temperature oxidation resistance, corrosion resistance, wear resistance, area-specific resistance (for SOFC applications), and hardness:

 doi:10.20944/preprints202509.1363.v1

(1) High-temperature oxidation resistance. Feng et al. [97,98] researched HEMAA-$LaCrO_3$ coatings after oxidation at 850°C for 200 h in air. The three-layer structure ($NiFe_2O_4$ outer layer inhibiting Cr volatilization, conductive $LaCrO_3$ middle layer, Cr_2O_3 inner layer resisting oxidation) exhibits a significantly lower oxidation rate than uncoated steel (mass gain: ~0.5 mg/cm² vs. 2.0 mg/cm² for uncoated steel), with ASR of 0.035-0.055 Ω·cm² (uncoated steel: 0.1 Ω·cm²) [97]. For HEMAA-FeAl coatings, after oxidation at 800-1000°C for 100 h in air, Al diffusion forms dense Al_2O_3 protective films, outperforming FeAl electrodes [99].

(2) Corrosion and wear resistance. Kumruoglu et al. [11] explored the potential of wire arc spraying technology to prepare Al-Mg6, Al-Si12, and pure Al coatings on low carbon steel surfaces, and further enhanced the corrosion and wear resistance of the coatings through MAO to address the issues of steel materials being prone to corrosion or wear. Hardness tests indicated that the Al-Si12 coating (140 Hk) exhibited the highest hardness, followed by Al-Mg6 (80 Hk), and pure Al (45 Hk) the lowest, with MAO significantly enhancing the coating hardness. High-performance composite coatings were successfully prepared on the surface of S355 offshore steel by combining laser cladding with micro-arc oxidation [12]. When the micro-arc oxidation current density was 5 A/dm², the coating exhibits the optimal overall performance: high hardness (1424.3 HV 0.2), good bonding strength (28.4 N), and remarkable corrosion resistance (corrosion current density of 1.21×10^{-8} A/cm²). This effectively inhibits the synergistic damage of corrosion-wear in the marine environment, providing a new technical solution for the protection of offshore steel [12].

(3) Area-specific resistance (ASR). After oxidation to form $LaCrO_3$ coatings, ASR remains < 40 mΩ·cm² for 500 h, far lower than uncoated steel (288 mΩ·cm²), meeting SOFC requirements (≤ 0.1 Ω·cm²) [97].

(4) Hardness and mechanical properties. The average thickness of the ESD coating is 17.5 ± 3 μm, while that of the duplex coating is 32.3 ± 5 μm (significantly thickened by MAO) [102]. Hardness values follow the order: St35 steel (270 HV) < ESD coating (510 HV) < duplex coating (940 HV). The enhanced hardness of the duplex coating is primarily attributed to the formation of α-Al_2O_3 (with a theoretical hardness of 2500 HV). Scratch test results show that the critical loads of the duplex coating (Lc1 = 29.530 N, Lc3 = 50.932 N) are significantly higher than those of the ESD coating (Lc1 = 15.199 N, Lc3 = 36.123 N), due to its greater thickness and hardness, which improve load-bearing capacity [102]. For uncoated steel, the friction coefficient rapidly increases in the initial stage and then stabilizes; for both ESD and duplex coatings, the friction coefficient is higher in the initial stage (attributed to their porous and rough surfaces), but stabilizes to a lower level than that of uncoated steel, demonstrating superior wear resistance [102].

3. Summary and Outlook

3.1. Summary

MAO, also known as plasma electrolytic oxidation, has emerged as a versatile electrochemical surface modification technique for fabricating in-situ ceramic coatings on diverse metallic materials, including lightweight alloys (Al, Mg, Ti), high-entropy alloys (HEAs), and steel (via hybrid processes). This review systematically synthesizes recent advancements in MAO technology, focusing on material-specific processing strategies, coating performance optimization, and critical challenges, and outlines future research directions to expand its industrial applications [1–3].

Aluminum alloys: MAO enables rapid formation of dense α-Al_2O_3/γ-Al_2O_3 coatings (10–100 μm thick) with hardness up to 2500 HV, significantly enhancing wear resistance (wear rate: $3.00–5.00 \times 10^{-6}$ mm³/N·m) and corrosion protection [6,25,33]. Electrolyte additives (e.g., SiC, graphene) and process controls (current density, ultrasonic assistance) further optimize densification, reducing porosity to < 2% and extending salt spray resistance (e.g., 530 h with 1.5 mg/cm² mass loss) [26,32].

Magnesium alloys: MAO addresses Mg's poor corrosion and wear resistance by forming bilayer coatings (inner dense MgO/Mg_2SiO_4, outer porous layer). Electrolyte systems (silicate, aluminate, phosphate) and post-treatments (laser melting, sealing) enhance corrosion resistance (e.g., reducing jcorr from 43.52 μA/cm² to 0.351 μA/cm² in aluminate-fluoride electrolytes) [53,57]. Bioactive MAO

 doi:10.20944/preprints202509.1363.v1

coatings (Ca/P-doped) on Mg alloys exhibit excellent biocompatibility (cell survival > 95%) and promote bone integration, making them promising for biodegradable implants [62,64].

Titanium alloys: MAO generates porous TiO_2-based coatings (anatase/rutile) with tailored bioactivity. Calcium-phosphate electrolytes enable hydroxyapatite (HA) formation, while Ag/Cu doping confers antibacterial properties (inhibition > 95% against S. aureus) [76]. UV-irradiated MAO coatings achieve superhydrophilicity (contact angle 0°), accelerating apatite nucleation in simulated body fluid (SBF) within 13–17 days [80]. These coatings also improve titanium-porcelain bonding strength (39.6% increase) and high-temperature oxidation resistance (stable at 800°C) [83,85].

High-entropy alloys (HEAs): MAO mitigates HEAs' poor high-temperature oxidation by forming composite oxide layers (Al_2O_3, Cr_2O_3, SiO_2) that suppress volatile oxide (V_2O_5, MoO_3) formation. Optimized electrolytes (Na_2SiO_3, $Na_2B_4O_7$) and voltage controls (420 V) reduce porosity and surface roughness (from 16.5 μm to 7.2 μm), lowering oxidation mass gain (e.g., from 12.91 mg/cm² to 8.67 mg/cm² for $AlTiNbMo_{0.5}Ta_{0.5}Zr$) [91,94].

Steel: Direct MAO is hindered by steel's high conductivity, but hybrid processes (pretreatment + MAO) enable ceramic coating growth. Techniques like hot-dip aluminizing, laser cladding, and high-energy micro-arc alloying (HEMAA) form valve metal interlayers (Al, FeAl), followed by MAO to produce Al_2O_3-based coatings. These hybrid coatings enhance high-temperature oxidation resistance (mass gain < 0.5 mg/cm² vs. 2.0 mg/cm² for uncoated steel), corrosion resistance (j_{corr} = 1.21 × 10^{-8} A/cm²), and hardness (up to 1424 HV) [97,102].

Figure 18 visually presents the results of this analysis from the Web of Science database, where the size of nodes in the network diagram is positively correlated with keyword frequency. Notably, "micro-arc oxidation", "microstructure" and "behavior" emerge as the most frequent keywords. By integrating the case study with bibliometric analysis, the critical value of micro-arc oxidation modification is fully highlighted. This comprehensive research approach emphasizes that an in-depth understanding of coating microstructure and behavioral mechanisms is imperative to enhance substrate surface performance through optimized micro-arc oxidation process design.

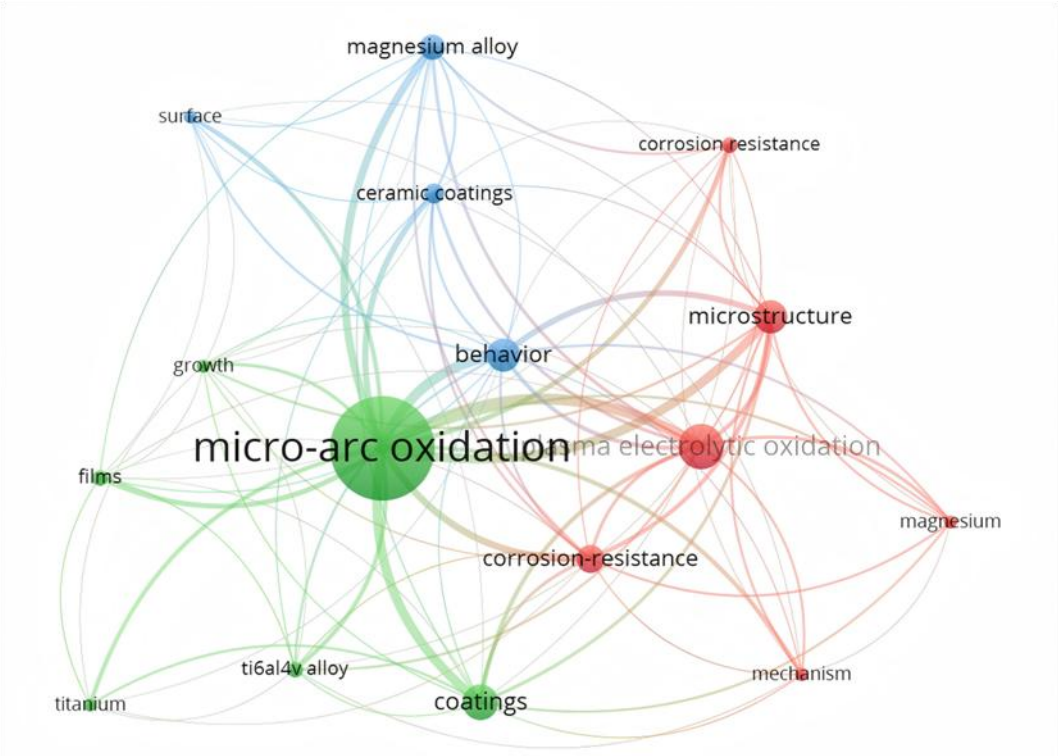

Figure 18. An overview of the research on micro-arc oxidation, the keyword network visualization literature from the Web of Science database.

 doi:10.20944/preprints202509.1363.v1

3.2. Outlook

Despite progress, critical challenges persist: (1) Coating uniformity: Complex geometries (e.g., aerospace components) suffer from uneven thickness and porosity due to localized discharge dynamics [39]. (2) Efficiency and scalability: Traditional MAO struggles with large-area or intricate parts; emerging scanning MAO (SMAO) and ultrasonic assistance processes show promise but require further optimization [37,38]. (3) Long-term stability: Residual stresses and microdefects (pores, cracks) compromise fatigue life and high-temperature durability [2]. (4) Environmental sustainability: Current electrolytes often contain hazardous components (e.g., strong alkalis); eco-friendly systems (biodegradable additives, low-toxicity salts) demand development [26,32].

Future research directions: (1) Multifunctional coatings: Efforts should focus on integrating self-healing (via encapsulated corrosion inhibitors), antibacterial (Ag/Cu doping), and tribological (graphene/SiC reinforcement) properties to meet demands in biomedical, aerospace, and energy sectors. (2) Eco-friendly electrolytes: Key strategies include designing low-pH, non-toxic electrolytes (e.g., phosphate-free, bio-derived stabilizers) to reduce environmental impact without sacrificing coating quality. (3) Mechanistic understanding: Critical steps include advanced characterization (e.g., operando XRD, in-situ Raman spectroscopy) and computational modeling (DFT, phase-field simulations) to clarify discharge dynamics, oxide growth mechanisms, and interface bonding. (4) Process innovation: Scalable techniques such as robotic SMAO and hybrid energy fields (ultrasonic, magnetic fields) aim to enhance uniformity and efficiency for large/complex components.

In summary, MAO technology has transformed surface engineering of metals, offering tailored solutions for corrosion, wear, and functionalization. By addressing current challenges and advancing interdisciplinary research, MAO is poised to unlock new applications in next-generation materials, ranging from biodegradable medical implants to high-temperature aerospace components.

Author Contributions: Writing—original draft preparation, N.N. L.; conceptualization, N.N. L, H.Y. W, Z.J. H., D. X., L. X. and X. C.; methodology, N.N. L., H.Y. W, Z.J. H, Q.Z. L., X. C. and Y.Y. F.; writing—review and editing, L. X. and Y.Y. F.; investigation, N.N. L., H.Y. W, Z.J. H, D. X., Q.Z. L, D.T. C, and Y.Y. F.; formal analysis, N.N. L, H.Y. W, Z.J. H, D. X., Q.Z. L, D.T. C, X. C. and L. X.; data curation, H.Y. W, Z.J. H, D. X., Q.Z. L, D.T. C, and L. X.; resources, H.Y. W, Z.J. H, D. X., Q.Z. L, and Y.Y. F.; supervision L. X. and Y.Y. F. All authors have read and agreed to the published version of the manuscript.

Funding: This work was financially supported by the Key R & D and Promotion Project of the Henan Province (Science and Technology Research) (Nos. 252102220078), the "Deputy General Manager of Technology" of Henan Province (HNFZ 20240193)

Institutional Review Board Statement: Not applicable

Informed Consent Statement: Not applicable

Data Availability Statement: The data presented in this study are available on request from the corresponding author

Conflicts of Interest: The authors declare no conflicts of interest.

References

1. Golubkov, P.E.; Pecherskaya, E.A.; Artamonov, D.V.; Zinchenko, T.O.; Gerasimova, Y.E.; Rozenberg, N.V. Electrophysical model of the micro-arc oxidation process. *Russ. Phys. J.*, **2020,** *62*, 2137-2144. https://doi.org/10.1007/s11182-020-01958-z.
2. Dai, W.B.; Zhang, C.; Yue, H.T.; Li, Q.; Guo, C.G.; Zhang, J.Z.; Zhao, G.C.; Yang, X.L. A review on the fatigue performance of micro-arc oxidation coated Al alloys with micro-defects and residual stress. *J. Mater. Res. Technol.*, **2023**, 25, 4554-4581. https://doi.org/10.1016/j.jmrt.2023.06.244.
3. Lin, Z.; Wang, T.; Yu, X.; Sun, X.; Yang, H. Functionalization treatment of micro-arc oxidation coatings on magnesium alloys: A review. *J. Alloy. Compd.*, **2021**, 879, 160453. https://doi.org/10.1016/j.jallcom.2021.160453.

 doi:10.20944/preprints202509.1363.v1

4. Ming, X.; Wu, Y.; Zhang, Z.; Li, Y. Micro-arc oxidation in titanium and its alloys: Development and potential of implants. *Coatings*, **2023**, 13(12), 2064. https://doi.org/ 10.3390/coatings13122064.
5. dos Santos, R. F.; Kuroda, P. A.; de Almeida, G. S.; Zambuzzi, W. F.; Grandini, C. R.; Afonso, C. R. New MAO coatings on multiprincipal equimassic β TiNbTaZr and TiNbTaZrMo alloys. *BME Adv.*, **2025**, 9, 100139. https://doi.org/10.1016/j.bea.2024.100139.
6. Tian, J.; Luo, Z.; Qi, S.; Sun, X. Structure and antiwear behavior of micro-arc oxidized coatings on aluminum alloy. *Surf. Coat. Tech.*, **2002**, 154(1), 1-7. https://doi.org/10.1016/S0257-8972(01)01671-1.
7. Duan, H.P.; Du, K.Q.; Yan, C.W.; Wang, F.H. Electrochemical corrosion behavior of composite coatings of sealed MAO film on magnesium alloy AZ91D. *Electrochim. Acta*, **2006**, 51(14), 2898-2908. https://doi.org/10.1016/j.electacta.2005.08.026.
8. Sun, X.T.; Jiang, Z.H.; Yao, Z.P.; Zhang, X.L. The effects of anodic and cathodic processes on the characteristics of ceramic coatings formed on titanium alloy through the MAO coating technology. *Appl. Surf. Sci.*, **2005**, 252(2), 441-447. https://doi.org/10.1016/j.apsusc.2005.01.023.
9. Yang, F.; Du, C.; Tao, S.Y.; Chang, Y.Q.; Nie, Z.H.; Wang, Z.; Lu, H.L. Study on the effect and growth mechanism of micro-arc oxidation coating on AlCoCrFeNi high entropy alloy. *J. Alloy. Compd.*, **2025**, 1020, 179469. https://doi.org/10.1016/j.jallcom.2025.179469.
10. Wang, S.P.; Zhou, L.; Li, C.J.; Li, Z.X.; Li, H.Z.; Yang, L.J. Micrographic properties of composite coatings prepared on TA2 substrate by hot-dipping in Al-Si alloy and using micro-arc oxidation technologies (MAO). *Coatings*, **2020**, 10(4), 374. https://doi.org/10.3390/coatings10040374.
11. Kumruoglu, L.C.; Ustel, F.; Ozel, A.; Mimaroglu, A. Micro arc oxidation of wire arc sprayed Al-Mg6, Al-Si12, Al coatings on low alloyed steel. *Engineering-PRC*, **2011**, 3(7), 680-690. https://doi.org/10.4236/eng.2011.37081.
12. He, X.; Song, R.G.; Kong, D.J. Microstructure and corrosion behaviours of composite coatings on S355 offshore steel prepared by laser cladding combined with micro-arc oxidation. *Appl. Surf. Sci.*, **2019**, 497, 143703. https://doi.org/10.1016/j.apsusc.2019.143703.
13. Yang, C.; Sun, Z.M.; Wang, C.Y.; Huang, A.H.; Ye, Z.S.; Ying, T.; Zhou, L.P.; Xiao, S.; Chu, P.K.; Zeng, X.Q. A self-sealing and self-healing MAO corrosion-resistant coating on aluminum alloy by in situ growth of $CePO_4/Al_2O_3$. *Corros. Sci.*, **2025**, 245, 112706. https://doi.org/10.1016/j.corsci.2025.112706.
14. Wang, S.; Gu, Y.; Geng, Y.; Liang, J.; Zhao, J.; Kang, J. Investigating local corrosion behavior and mechanism of MAO coated 7075 aluminum alloy. *J. Alloy. Compd.*, **2020**, 826, 153976. https://doi.org/10.1016/j.jallcom.2020.153976.
15. Liu, X.; Zhu, L.; Liu, H.; Li, W. Investigation of MAO coating growth mechanism on aluminum alloy by two-step oxidation method. *Appl. Surf. Sci.*, **2014**, 293, 12-17. https://doi.org/10.1016/j.apsusc.2013.11.159.
16. Tseng, C. C.; Lee, J. L.; Kuo, T. H.; Kuo, S. N.; Tseng, K. H. The influence of sodium tungstate concentration and anodizing conditions on microarc oxidation (MAO) coatings for aluminum alloy. *Surf. Coat. Tech.*, **2012**, 206(16), 3437-3443. https://doi.org/10.1016/j.surfcoat.2012.02.002.
17. Wang, J.; Huang, S.; Huang, H.; He, M.; Wangyang, P.; Gu, L. Effect of micro-groove on microstructure and performance of MAO ceramic coating fabricated on the surface of aluminum alloy. *J. Alloy. Compd.*, **2019**, 777, 94-101. https://doi.org/10.1016/j.jallcom.2018.10.374.
18. Huang, H.; Wei, X.; Yang, J.; Wang, J. Influence of surface micro grooving pretreatment on MAO process of aluminum alloy. *Appl. Surf. Sci.*, **2016**, 389, 1175-1181. https://doi.org/10.1016/j.apsusc.2016.08.088.
19. Shehadeh, L.; Mohamed, K.; Al-Qawabeha, U.; Abu-Jdayil, B. The Role of Copper Incorporation in Improving the Electrical Insulation Properties of Microarc Oxidation Coatings on Aluminum Alloys. *Eng. Sci.*, **2025**, 33, 1380. https://doi.org/10.30919/es1380.
20. Wang, G.; Zhang, Y.; Li, J.; Zhao, J.; Ma, C.; Zhao, G. Analysis of frictional performance of microarc oxidized aluminum alloys in various media: Integration of experimental and MD simulation approaches. *Mater. Today. Commun.*, **2025**, 46, 112528. https://doi.org/10.1016/j.mtcomm.2025.112528.
21. Yin, J. H.; Cui, Y. W.; Shang, Y. Y.; Lu, L. H.; Du, R. W.; Zhu, M. Investigation of third harmonic laser-induced damage on micro-arc oxidized and composite-coated aluminum alloy 7075. *J. Alloy. Compd.*, **2025**, 1032, 181087. https://doi.org/10.1016/j.jallcom.2025.181087.

 doi:10.20944/preprints202509.1363.v1

22. Yu, D. L.; Jiang, B.; Qi, X.; Wang, C.; Song, R. G. Effect of current density on microstructure, mechanical behavior and corrosion resistance of black MAO coating on 6063 aluminum alloy. *Mater. Chem. Phys.*, **2024**, 326, 129800. https://doi.org/10.1016/j.matchemphys.2024.129800.
23. Long, B. H.; Wu, H. H.; Long, B. Y.; Wang, J. B.; Wang, N. D.; Lü, X. Y.; Jin, Z.S.; Bai, Y. Z. Characteristics of electric parameters in aluminium alloy MAO coating process. *J. Phys. D. Appl. Phys.*, **2005**, 38(18), 3491. https://doi.org/10.1088/0022-3727/38/18/025.
24. Li, H. X.; Li, W. J.; Song, R. G.; Ji, Z. G. Effects of different current densities on properties of MAO coatings embedded with and without α-Al_2O_3 nanoadditives. *Mater.Sci. Tech.-Lond*, **2012**, 28(5), 565-568. https://doi.org/10.1179/1743284711Y.0000000084.
25. Yang, G.L.; Lü, X.Y.; Bai, Y.Z.; Cui, H.F.; Jin, Z.S. The effects of current density on the phase composition and microstructure properties of micro-arc oxidation coating. *J. Alloy. Compd.*, **2002**, 345(1-2), 196-200. https://doi.org/10.1016/S0925-8388(02)00289-X.
26. Wang, P.; Wu, T.; Xiao, Y.T.; Zhang, L.; Pu, J.; Cao, W.J.; Zhong, X.M. Characterization of micro-arc oxidation coatings on aluminum drillpipes at different current density. *Vacuum*, **2017**, 142, 21-28. https://doi.org/10.1016/j.vacuum.2017.04.038.
27. Wang, J.H.; Du, M.H.; Han, F.Z.; Yang, J. Effects of the ratio of anodic and cathodic currents on the characteristics of micro-arc oxidation ceramic coatings on Al alloys. *Appl. Surf. Sci.*, **2014**, 292, 658-664. https://doi.org/10.1016/j.apsusc.2013.12.028.
28. Tran, Q.P.; Kuo, Y.C.; Sun, J.K.; He, J.L.; Chin, T.S. High quality oxide-layers on Al-alloy by micro-arc oxidation using hybrid voltages. *Surf. Coat. Tech.*, **2016**, 303, 61-67. https://doi.org/10.1016/j.surfcoat.2016.03.049.
29. Li, X.Y.; Li, X.G.; Li, Y.; Dong, C.F.; Tian, H.P.; Wang, S.X.; Zhao, Q. Growth mechanism of micro-arc oxidation film on 6061 aluminum alloy. *Mater. Res. Express*, **2019**, 6(6), 066404. http://dx.doi.org/10.1088/2053-1591/ab0a20.
30. Jin. F.Y.; Chu, P.K.; Tong, H.H., Zhao, J. Improvement of surface porosity and properties of alumina films by incorporation of Fe micrograins in micro-arc oxidation. *Appl. Surf. Sci.*, **2006**, 253(2), 863-868. https://doi.org/10.1016/j.apsusc.2006.01.024.
31. Li, W.P.; Qian, Z.Y.; Liu, X.H.; Zhu, L.Q.; Liu, H.C. Investigation of micro-arc oxidation coating growth patterns of aluminum alloy by two-step oxidation method. *Appl. Surf. Sci.*, **2015**, 356, 581-586. https://doi.org/10.1016/j.apsusc.2015.07.005.
32. Chen, Q.Z.; Jiang, Z.Q.; Tang, S.G.; Dong, W.B.; Tong, Q.; Li, W.Z. Influence of graphene particles on the micro-arc oxidation behaviors of 6063 aluminum alloy and the coating properties. *Appl. Surf. Sci.*, **2017**, 423, 939-950. https://doi.org/10.1016/j.apsusc.2017.06.202.
33. Arslan, E.; Totik, Y.; Demirci, E.E.; Vangolu, Y.; Alsaran, A.; Efeoglu, I. High temperature wear behavior of aluminum oxide layers produced by AC micro arc oxidation. *Surf. Coat. Tech.*, **2009**, 204(6-7), 829-833. https://doi.org/10.1016/j.surfcoat.2009.09.057.
34. Li, Z.Y.; Cai, Z.B.; Cui, Y.; Liu, J.H.; Zhu, M.H. Effect of oxidation time on the impact wear of micro-arc oxidation coating on aluminum alloy. *Wear*, **2019**, 426, 285-295. https://doi.org/10.1016/j.wear.2019.01.084.
35. Venugopal, A.; Panda, R.; Manwatkar, S.; Sreekumar, K.; Krishna, L. R.; Sundararajan, G. Effect of micro arc oxidation treatment on localized corrosion behaviour of AA7075 aluminum alloy in 3.5% NaCl solution. *T. Nonferr. Metal. Soc.*, **2012**, 22(3), 700-710. https://doi.org/10.1016/S1003-6326(11)61234-X.
36. Xin, S.G.; Song, L.X.; Zhao, R.G.; Hu, X.F. Properties of aluminium oxide coating on aluminium alloy produced by micro-arc oxidation. *Surf. Coat. Tech.*, **2005**, 199(2-3), 184-188. https://doi.org/10.1016/j.surfcoat.2004.11.044.
37. Ma, G.F.; Li, Z.P.; Zhao, X.R.; Wang, Z.Y.; Sun, S.N.; Yang, Y.H.; Sun, Y.; Wang, S.Y.; Ren, S.T.; Kou, R.H. Growth mechanism and product formation of Micro-arc oxide film layers on aluminum matrix composites: An analytical experimental and computational simulation study. *Appl. Surf. Sci.*, **2025**, 684, 161968. https://doi.org/10.1016/j.apsusc.2024.161968.
38. Liu, Z.H.; Lu, H.L.; Zhao, Z.Y.; Zhu, Z.Q.; Li, S.B. Influence of ultrasonic power modulation on the optimisation of aluminium alloy micro-arc oxidation coating properties. *Appl. Surf. Sci.*, **2025**, 679, 161067. https://doi.org/10.1016/j.apsusc.2024.161067.

 doi:10.20944/preprints202509.1363.v1

39. Zhu, Z.Q.; Lu, H.L.; Shen, T.J.; Wang, Z.Z.; Xu, G.S.; Liu, Z.H.; Yang, H. Performance study of scanning micro-arc oxidation ceramic coatings on aluminum alloys based on different electrolyte flow rates. *Surf. Coat. Tech.*, **2025**, 496, 131686. https://doi.org/10.1016/j.surfcoat.2024.131686.
40. Zhu, Z.Q.; Li, S.B.; Xue, Z.C.; Liu, Z.H.; Tu, N.; Lu, H.L. Performance evaluation of scanning micro-arc oxidation ceramic coating on aluminum alloy under different current working modes. *Mater. Chem. Phys.*, **2025**, 336, 130538. https://doi.org/10.1016/j.matchemphys.2025.130538.
41. Narayanan, T. S.; Park, I. S.; Lee, M. H. Strategies to improve the corrosion resistance of microarc oxidation (MAO) coated magnesium alloys for degradable implants: Prospects and challenges. *Prog. Mater. Sci.*, **2014**, 60, 1-71. https://doi.org/10.1016/j.pmatsci.2013.08.002.
42. Zhang, R. F.; Zhang, S. F.; Duo, S. W. Influence of phytic acid concentration on coating properties obtained by MAO treatment on magnesium alloys. *Appl. Surf. Sci.*, **2009**, 255(18), 7893-7897. https://doi.org/10.1016/j.apsusc.2009.04.145.
43. Li, Z.; Yu, Q.; Zhang, C.; Liu, Y.; Liang, J.; Wang, D.; Zhou, F. Synergistic effect of hydrophobic film and porous MAO membrane containing alkynol inhibitor for enhanced corrosion resistance of magnesium alloy. *Surf. Coat. Tech.*, **2019**, 357, 515-525. https://doi.org/10.1016/j.surfcoat.2018.10.054.
44. Ezhilselvi, V.; Nithin, J.; Balaraju, J. N.; Subramanian, S. The influence of current density on the morphology and corrosion properties of MAO coatings on AZ31B magnesium alloy. *Surf. Coat. Tech.*, **2016**, 288, 221-229. https://doi.org/10.1016/j.surfcoat.2016.01.040.
45. Guo, C.; Li, Y.; Qi, C.; Sun, H.; Zhang, D.; Wan, Y. Effect of solvent acids on the microstructure and corrosion resistance of chitosan films on MAO-treated AZ31B magnesium alloy. *Int. J. Biol. Macromol.*, **2024**, 277, 134349. https://doi.org/10.1016/j.ijbiomac.2024.134349.
46. Dou, J.; Yu, H.; Chen, C.; Ma, R. L. W.; Yuen, M. M. F. Preparation and microstructure of MAO/CS composite coatings on Mg alloy. *Mater. Lett.*, **2020**, 271, 127729. https://doi.org/10.1016/j.matlet.2020.127729.
47. Ungan, G.; Cakir, A. Investigation of MgO effect on bioactivity of coatings produced by MAO. *Surf. Coat. Tech.*, **2015**, 282, 52-60. https://doi.org/10.1016/j.surfcoat.2015.09.053.
48. Liu, C.; Zhang, W.; Xu, T.; Li, H.; Jiang, B.; Miao, X. Preparation and corrosion resistance of a self-sealing hydroxyapatite-MgO coating on magnesium alloy by microarc oxidation. *Ceram. Int.*, **2022**, 48(10), 13676-13683. https://doi.org/10.1016/j.ceramint.2022.01.249.
49. Vladimirov, B. V.; Krit, B. L.; Lyudin, V. B.; Morozova, N. V.; Rossiiskaya, A. D.; Suminov, I. V.; Epel'Feld, A. V. Microarc oxidation of magnesium alloys: A review. *Surf. Eng. Appl. Electrochem.*, **2014**, 50, 195-232. https://doi.org/10.3103/S1068375514030090.
50. Pesode, P.; Barve, S.; Dayane, S. Antibacterial coating on magnesium alloys by MAO for biomedical applications. *Res. Biomed. Eng.*, **2024**, 40(2), 409-433. https://doi.org/10.1007/s42600-024-00347-6.
51. Xiong, Y.; Lu, C.; Wang, C.; Song, R. Degradation behavior of n-MAO/EPD bio-ceramic composite coatings on magnesium alloy in simulated body fluid. *J. Alloy. Compd.*, **2015**, 625, 258-265. https://doi.org/10.1016/j.jallcom.2014.11.084.
52. Razavi, M.; Fathi, M.; Savabi, O.; Vashaee, D.; Tayebi, L. Biodegradable magnesium alloy coated by fluoridated hydroxyapatite using MAO/EPD technique. *Surf. Eng.*, **2014**, 30(8), 545-551. https://doi.org/10.1179/1743294414Y.0000000284.
53. Guo, H.F.; An, M.Z.; Xu, S.; Huo, H.B. Formation of oxygen bubbles and its influence on current efficiency in micro-arc oxidation process of AZ91D magnesium alloy. *Thin Solid Films*, **2005**, 485(1-2), 53-58. https://doi.org/10.1016/j.tsf.2005.03.050.
54. Guo, H. F.; An, M. Z.; Huo, H. B.; Xu, S.; Wu, L. J. Microstructure characteristic of ceramic coatings fabricated on magnesium alloys by micro-arc oxidation in alkaline silicate solutions. *Appl. Surf. Sci.*, **2006**, 252(22), 7911-7916. https://doi.org/10.1016/j.apsusc.2005.09.067.
55. Zhang, R. F.; Zhang, S. F. Formation of micro-arc oxidation coatings on AZ91HP magnesium alloys. *Corros. Sci.*, **2009**, 51(12), 2820-2825. https://doi.org/10.1016/j.corsci.2009.08.009.
56. Tang, H.; Han, Y.; Wu, T.; Tao, W.; Jian, X.; Wu, Y.; Xu, F. Synthesis and properties of hydroxyapatite-containing coating on AZ31 magnesium alloy by micro-arc oxidation. *Appl. Surf. Sci.*, **2017**, 400, 391-404. https://doi.org/10.1016/j.apsusc.2016.12.216.

 doi:10.20944/preprints202509.1363.v1

57. Guo, H. F.; An, M. Z. Growth of ceramic coatings on AZ91D magnesium alloys by micro-arc oxidation in aluminate–fluoride solutions and evaluation of corrosion resistance. *Appl. Surf. Sci*, **2005**, 246(1-3), 229-238. https://doi.org/10.1016/j.apsusc.2004.11.031.
58. Zhao, L.C.; Cui, C.X.; Wang, Q.Z.; Bu, S.J. Growth characteristics and corrosion resistance of micro-arc oxidation coating on pure magnesium for biomedical applications. *Corros. Sci.*, **2010**, 52(7), 2228-2234. https://doi.org/10.1016/j.corsci.2010.03.008.
59. Durdu, S.; Aytac, A.; Usta, M. Characterization and corrosion behavior of ceramic coating on magnesium by micro-arc oxidation. *J. Alloy. Compd.*, **2011**, 509(34), 8601-8606. https://doi.org/10.1016/j.jallcom.2011.06.059.
60. Muhaffel, F.; Cimenoglu, H. Development of corrosion and wear resistant micro-arc oxidation coating on a magnesium alloy. *Surf. Coat. Tech.*, **2019**, 357, 822-832. https://doi.org/10.1016/j.surfcoat.2018.10.089.
61. Durdu, S.; Usta, M. Characterization and mechanical properties of coatings on magnesium by micro arc oxidation. *Appl. Surf. Sci.*, **2012**, 261, 774-782. https://doi.org/10.1016/j.apsusc.2012.08.099.
62. Pan, Y. K.; Chen, C. Z.; Wang, D. G.; Yu, X. Microstructure and biological properties of micro-arc oxidation coatings on ZK60 magnesium alloy. *J. Biomed. Mater. Res. B*, **2012**, 100(6), 1574-1586. https://doi.org/10.1002/jbm.b.32726.
63. Pan, Y. K.; Chen, C. Z.; Wang, D. G.; Lin, Z. Q. Preparation and bioactivity of micro-arc oxidized calcium phosphate coatings. *Mater. Chem. Phys.*, **2013**, 141(2-3), 842-849. https://doi.org/10.1016/j.matchemphys.2013.06.013.
64. Ma, W. H.; Liu, Y. J.; Wang, W.; Zhang, Y. Z.. Improved biological performance of magnesium by micro-arc oxidation. *Braz. J. Med. Biol. Res.*, **2015**, 48(3), 214-225. https://doi.org/10.1590/1414-431X20144171.
65. Zhang, Z. Q.; Wang, L.; Zeng, M. Q.; Zeng, R. C.; Kannan, M. B.; Lin, C. G.; Zheng, Y. F. Biodegradation behavior of micro-arc oxidation coating on magnesium alloy-from a protein perspective. *Bioact. Mater.*, **2020**, 5(2), 398-409. https://doi.org/10.1016/j.bioactmat.2020.03.005.
66. Shao, Y.; Han, X.; Ma, C.; Wei, Y.; Zhu, X.; Xu, J. The thermal dynamic simulation and microstructure characterization of micro-arc oxidation (MAO) films on magnesium AZ31 irradiated by high-intensity pulsed ion beam. *Appl. Surf. Sci.*, **2025**, 682, 161705. https://doi.org/10.1016/j.apsusc.2024.161705.
67. Li, Y.; Yang, C.; Zhao, H.; Qu, S.; Li, X.; Li, Y. New developments of Ti-based alloys for biomedical applications. *Materials*, **2014**, 7(3), 1709-1800. https://doi.org/10.3390/ma7031709.
68. Geetha, M.; Singh, A. K.; Asokamani, R.; Gogia, A. K. Ti based biomaterials, the ultimate choice for orthopaedic implants-A review. *Prog. Mater. Sci.*, **2009**, 54(3), 397-425. https://doi.org/10.1016/j.pmatsci.2008.06.004.
69. Zhu, S. L.; Wang, X. M.; Qin, F. X.; Inoue, A. A new Ti-based bulk glassy alloy with potential for biomedical application. *Mater. Sci. Eng. A*, **2007**, 459(1-2), 233-237. https://doi.org/10.1016/j.msea.2007.01.044.
70. Liao, S. C.; Chang, C. T.; Chen, C. Y.; Lee, C. H.; Lin, W. L. Functionalization of pure titanium MAO coatings by surface modifications for biomedical applications. *Surf. Coat. Tech.*, **2020**, 394, 125812. https://doi.org/10.1016/j.surfcoat.2020.125812.
71. Xi, F.Q.; Zhang, X.W.; Kang, Y.Y.; Wen, X.Y.; Liu, Y. Mechanistic analysis of improving the corrosion performance of MAO coatings on Ti-6Al-4V alloys by annealing. *Surf. Coat. Tech.*, **2024**, 476, 130264. https://doi.org/10.1016/j.surfcoat.2023.130264.
72. Kuroda, P. A. B.; Rossi, M. C.; Grandini, C. R.; Afonso, C. R. M. Assessment of applied voltage on the structure, pore size, hardness, elastic modulus, and adhesion of anodic coatings in Ca-, P-, and Mg-rich produced by MAO in Ti-25Ta-Zr alloys. *J. Mater. Res. Technol.*, **2023**, 26, 4656-4669. https://doi.org/10.1016/j.jmrt.2023.08.165.
73. Maj, Ł.; Muhaffel, F.; Jarzębska, A.; Trelka, A.; Trembecka-W´ojciga, K.; Kawałko, J.; Kulczyk, M.; Bieda, M.; Çimenoˇglu, H. Enhancing the tribological performance of MAO coatings through hydrostatic extrusion of cp-Ti. *J. Alloy. Compd.*, **2025**, 1010, 178246. https://doi.org/10.1016/j.jallcom.2024.178246.
74. Han, Y.; Sun, J.; Huang, X. Formation mechanism of HA-based coatings by micro-arc oxidation. *Electrochem. Commun.*, **2008**, 10(4), 510-513. https://doi.org/10.1016/j.elecom.2008.01.026.
75. Han, Y.; Hong, S. H.; Xu, K. Structure and in vitro bioactivity of titania-based films by micro-arc oxidation. *Surf. Coat. Tech.*, **2003**, 168(2-3), 249-258. https://doi.org/10.1016/S0257-8972(03)00016-1.

 doi:10.20944/preprints202509.1363.v1

76. Song, W. H.; Ryu, H. S.; Hong, S. H. Antibacterial properties of Ag (or Pt)-containing calcium phosphate coatings formed by micro-arc oxidation. *J. Biomed. Mater. Res. A*, **2009**, 88(1), 246-254. https://doi.org/10.1002/jbm.a.31877.
77. Li, H.; Sun, Y.; Zhang, J. Effect of ZrO_2 particle on the performance of micro-arc oxidation coatings on Ti6Al4V. *Appl. Surf. Sci.*, **2015**, 342, 183-190. https://doi.org/10.1016/j.apsusc.2015.03.051.
78. Yao, Z. Q.; Ivanisenko, Y.; Diemant, T.; Caron, A.; Chuvilin, A.; Jiang, J. Z.; Valiev, R.Z.; Qi, M.; Fecht, H. J. Synthesis and properties of hydroxyapatite-containing porous titania coating on ultrafine-grained titanium by micro-arc oxidation. *Acta Biomater.*, **2010**, 6(7), 2816-2825. https://doi.org/10.1016/j.actbio.2009.12.053.
79. Xu, L.; Wu, C.; Lei, X.; Zhang, K.; Liu, C.; Ding, J.; Shi, X. Effect of oxidation time on cytocompatibility of ultrafine-grained pure Ti in micro-arc oxidation treatment. *Surf. Coat. Tech.*, **2018**, 342, 12-22. https://doi.org/10.1016/j.surfcoat.2018.02.044.
80. Han, Y.; Chen, D.; Sun, J.; Zhang, Y.; Xu, K. UV-enhanced bioactivity and cell response of micro-arc oxidized titania coatings. *Acta Biomater*, **2008**, 4(5), 1518-1529. https://doi.org/10.1016/j.actbio.2008.03.005.
81. Kung, K. C.; Lee, T. M.; Lui, T. S. Bioactivity and corrosion properties of novel coatings containing strontium by micro-arc oxidation. *J. Alloy. Compd.*, **2010**, 508(2), 384-390. https://doi.org/10.1016/j.jallcom.2010.08.057.
82. Cimenoglu, H.; Gunyuz, M.; Kose, G. T.; Baydogan, M.; Uğurlu, F.; Sener, C. Micro-arc oxidation of Ti6Al4V and Ti6Al7Nb alloys for biomedical applications. *Mater. Charact.*, **2011**, 62(3), 304-311. https://doi.org/10.1016/j.matchar.2011.01.002.
83. Li, J. X.; Zhang, Y. M.; Han, Y.; Zhao, Y. M. Effects of micro-arc oxidation on bond strength of titanium to porcelain. *Surf. Coat. Tech.*, **2010**, 204(8), 1252-1258. https://doi.org/10.1016/j.surfcoat.2009.10.020.
84. Yao, J. H.; Wang, Y.; Wu, G. L.; Sun, M.; Wang, M.; Zhang, Q. L. Growth characteristics and properties of micro-arc oxidation coating on SLM-produced TC4 alloy for biomedical applications. *Appl. Surf. Sci.*, **2019**, 479, 727-737. https://doi.org/10.1016/j.apsusc.2019.02.142.
85. Hao, G. D.; Zhang, D. Y.; Lou, L. Y.; Yin, L. C. High-temperature oxidation resistance of ceramic coatings on titanium alloy by micro-arc oxidation in aluminate solution. *Prog. Nat. Sci.*, **2022**, 32(4), 401-406. https://doi.org/10.1016/j.pnsc.2022.06.001.
86. Zhou, Y. H.; Chen, P. H.; Huang, D. N.; Wu, Z. Z.; Yang, T.; Kai, J. J.; Yan, M. Micro-arc oxidation for improving high-temperature oxidation resistance of additively manufacturing Ti_2AlNb. *Surf. Coat. Tech.*, **2022**, 445, 128719. https://doi.org/10.1016/j.surfcoat.2022.128719.
87. George, E. P.; Raabe, D.; Ritchie, R. O. High-entropy alloys. *Nat. Rev. Mater*, **2019**, 4(8), 515-534. https://doi.org/10.1038/s41578-019-0121-4.
88. Miracle, D. B.; Senkov, O. N. A critical review of high entropy alloys and related concepts. *Acta Mater.*, **2017**, 122, 448-511. https://doi.org/10.1016/j.actamat.2016.08.081.
89. Li, W. D.; Xie, D.; Li, D. Y.; Zhang, Y.; Gao, Y. F.; Liaw, P. K. Mechanical behavior of high-entropy alloys. *Prog. Mater. Sci.*, **2021**, 118, 100777. https://doi.org/10.1016/j.pmatsci.2021.100777.
90. Cheng, Z.; Yang, W.; Xu, D.; Shao, W.; Chen, J. In situ formation of micro arc oxidation ceramic coating on refractory high entropy alloy. *Int. J. Refract. Met. H.*, **2024**, 120, 106563. https://doi.org/10.1016/j.ijrmhm.2024.106563.
91. Cheng, Z. H.; Yang, W.; Xu, D. P.; Wu, S. K.; Yao, X. F.; Lv, Y. K.; Chen, J. Improvement of high temperature oxidation resistance of micro arc oxidation coated $AlTiNbMo_{0.5}Ta_{0.5}Zr$ high entropy alloy. *Mater. Lett.*, **2020**, 262, 127192. https://doi.org/10.1016/j.matlet.2019.127192.
92. Senkov, O. N.; Wilks, G. B.; Miracle, D. B.; Chuang, C. P.; Liaw, P. K. Refractory high-entropy alloys. *Intermetallics*, **2010**, 18(9), 1758-1765. https://doi.org/10.1016/j.intermet.2010.05.014.
93. Ye, F.X.; Jiao, Z. P.; Yan, S.; Guo, L.; Feng, L. Z.; Yu, J. X. Microbeam plasma arc remanufacturing: Effects of Al on microstructure, wear resistance, corrosion resistance and high temperature oxidation resistance of AlxCoCrFeMnNi high-entropy alloy cladding layer. *Vacuum*, **2020**, 174, 109178. https://doi.org/10.1016/j.vacuum.2020.109178.
94. Shi, X. Q.; Yang, W.; Cheng, Z. H.; Shao, W. T.; Xu, D. P.; Zhang, Y.; Chen, J. Influence of micro arc oxidation on high temperature oxidation resistance of AlTiCrVZr refractory high entropy alloy. *Int. J. Refract. Met. H.*, **2021**, 98, 105562. https://doi.org/10.1016/j.ijrmhm.2021.105562.

 doi:10.20944/preprints202509.1363.v1

95. Wang, Z.; Cheng, Z. H.; Zhang, Y.; Shi, X. Q.; Rao, M.; Wu, S.K. Effect of voltage on the microstructure and high-temperature oxidation resistance of micro-arc oxidation coatings on AlTiCrVZr refractory high-entropy alloy. *Coatings*, **2023**, 13(1), 14. https://doi.org/10.3390/coatings13010014.
96. Zhao, Z. H.; Chen, M. F.; You, C.; Li, W.; Tie, D.; Liu, H. F. Effect of α-Al_2O_3 additive on the microstructure and properties of MAO coatings prepared on low carbon steel. *J. Mater. Res. Technol*, **2020**, 9(3), 3875-3884. https://doi.org/10.1016/j.jmrt.2020.02.014.
97. Feng, Z. J.; Zeng, C. L. Oxidation behavior and electrical property of ferritic stainless steel interconnects with a Cr–La alloying layer by high-energy micro-arc alloying process. *J. Power Sources*, **2010**, 195(21), 7370-7374. https://doi.org/10.1016/j.jpowsour.2010.06.016.
98. Feng, Z. J.; Zeng, C. $LaCrO_3$-based coatings deposited by high-energy micro-arc alloying process on a ferritic stainless steel interconnect material. *J. Power Sources*, **2010**, 195(13), 4242-4246. https://doi.org/10.1016/j.jpowsour.2010.01.023.
99. Guo, P.; Shao, Y.; Zeng, C.; Wu, M.; Li, W. Oxidation characterization of FeAl coated 316 stainless steel interconnects by high-energy micro-arc alloying technique for SOFC. *Mater. Lett.*, **2011**, 65(19-20), 3180-3183. https://doi.org/10.1016/j.matlet.2011.06.032.
100. Lu, L. H.; Shen, D. J.; Zhang, J. W.; Song, J.; Li, L. Evolution of micro-arc oxidation behaviors of the hot-dipping aluminum coatings on Q235 steel substrate. *Appl. Surf. Sci.*, **2011**, 257(9), 4144-4150. https://doi.org/10.1016/j.apsusc.2010.11.187.
101. Wang, W. Z.; Feng, S. S.; Li, Z. M.; Chen, Z. G.; Zhao, T. Y. Microstructure and properties of micro-arc oxidation ceramic films on AerMet100 steel. *J. Mater. Res. Technol.*, **2020**, 9(3), 6014-6027. https://doi.org/10.1016/j.jmrt.2020.04.005.
102. Durdu, S.; Aktuğ, S. L.; Korkmaz, K. Characterization and mechanical properties of the duplex coatings produced on steel by electro-spark deposition and micro-arc oxidation. *Surf. Coat. Tech.*, **2013**, 236, 303-308. https://doi.org/10.1016/j.surfcoat.2013.10.004.
103. Durdu, S.; Korkmaz, K.; Aktuğ, S. L.; Çakır, A. Characterization and bioactivity of hydroxyapatite-based coatings formed on steel by electro-spark deposition and micro-arc oxidation. *Surf. Coat. Tech.*, **2017**, 326, 111-120. https://doi.org/10.1016/j.surfcoat.2017.07.039.
104. Sun, S. C.; Cheng, B.; Liu, A.; Liu, Z. H.; Xu, G. M.; Liu, P.; Lu, H. L. Research on micro-arc oxidation method based on passivation layer on non-valve metal low-carbon steel surface. *Tribol. Int.*, **2024**, 200, 110114. https://doi.org/10.1016/j.triboint.2024.110114.
105. Malinovschi, V.; Marin, A.; Moga, S.; Negrea, D. Preparation and characterization of anticorrosive layers deposited by micro-arc oxidation on low carbon steel. *Surf. Coat. Tech.*, **2014**, 253, 194-198. https://doi.org/10.1016/j.surfcoat.2014.05.036.
106. Li, Y.; Chen, M.; Li, W.; Wang, Q.; Wang, Y.; You, C. Preparation, characteristics and corrosion properties of α-Al_2O_3 coatings on 10B21 carbon steel by micro-arc oxidation. *Surf. Coat. Tech.*, **2019**, 358, 637-645. https://doi.org/10.1016/j.surfcoat.2018.11.094.